Quantification of combustion regime transitions in premixed turbulent DME flames

F. Hampp, R. P. Lindstedt*

Department of Mechanical Engineering, Imperial College, London, SW7 2AZ, UK

Abstract

The current study quantifies the probability of encountering up to five fluid states (reactants, combustion products, mixing fluid, fluids with low and high reactivity) in premixed turbulent DME flames as a function of the Damköhler number. The flames were aerodynamically stabilised in a back–to–burnt opposed jet configuration featuring fractal grid generated multi-scale turbulence ($Re \simeq 18{,}400$ and $Re_t > 370$). The chemical timescale was varied via the mixture stoichiometry resulting in a wide range of Damköhler numbers ($0.08 \leq Da \leq 5.6$). The mean turbulent strain ($\geq 3200\,\mathrm{s}^{-1}$) exceeded the extinction strain rate of the corresponding laminar flames for all mixtures. Simultaneous Mie scattering, OH-PLIF and PIV were used to identify the fluid states and supporting computations show that the thermochemical state (e.g. OH and CH concentrations) at the twin flame extinction point correlates well with flames in the back-to-burnt geometry at the corresponding rate of heat release. For mixtures where the bulk strain ($\simeq 750\,\mathrm{s}^{-1}$) was similar to (or less than) the extinction strain rate, fluids with low and high reactivity could accordingly be segregated by a threshold based on the OH concentration at the extinction point. A sensitivity analysis of the distribution between the fluid states was performed. The flow conditions were further analysed in terms of Damköhler and Karlovitz numbers. The study provides (i) the evolution of multi–fluid probability statistics as a function of the Damköhler number, including (ii) the flow direction across fluid interfaces and OH gradients, (iii) mean flow field statistics, (iv) conditional velocity statistics and (v) a tentative combustion regime classification.

Keywords: Combustion Regime Transition, DME, Multi–Fluid Statistics, Premixed Flames, Fractal Grid Generated Turbulence

*Corresponding author. Fax: +44 20 7594 5696.
Email address: p.lindstedt@imperial.ac.uk (R. P. Lindstedt)

Nomenclature

Roman Letters

A	Area [m^2].
A_{21}	Einstein spontaneous emission coefficient [s^{-1}].
a	Rate of strain [s^{-1}].
$\overline{c}$	Reaction progress variable [–].
c	Progress variable; Instantaneous conditioning variable [–].
D	Burner nozzle diameter [m].
Da	Conventional Damköhler number [–].
Da_b	Convective auto–ignition Damköhler number [–].
Da_{ign}	Turbulent auto–ignition Damköhler number [–].
$d_{p,x}$	Al_2O_3 particle diameter x% [m].
H	Burner nozzle separation [m].
I	Experimental fluorescence signal intensities [–].
I^{ν}	Laser irradiance [$W\,m^{-2}$].
$I^{\ddagger}$	Reference signal intensity [–].
Ka	Conventional Karlovitz number [–].
Ka_{ign}	Auto–ignition Karlovitz number [–].
$k_{v'J'v''J''}$	Absorption line strength [$W\,m^{-2}$].
[k]	Theoretical concentration of species k [mol/m^3].
L_{η}	Kolmogorov length scale [m].
L_I	Integral length scale of turbulence [m].
M	Optical magnification [–].
N	Total number of images [–].
N_{sd}	Particle seeding density [particles/unit volume].
n	Instantaneous image [–].
$\hat{\mathbf{n}}$	Unit vector of the iso-contour normal [–].
P	Pressure [Pa].
$\dot{Q}$	Heat release rate [$W\,m^{-3}$].
Q_{21}	Collisional quenching rate [s^{-1}].
Re_t	Turbulent Reynolds number [–].
S_f	Fluorescence power [photons/s].
S_L	Laminar burning velocity [$m\,s^{-1}$].
$\hat{\mathbf{s}}$	Unit vector of the streamline tangent [–].
T	Temperature [K].
T_{ad}	Adiabatic flame temperature [K].
T_{ign}	Auto–ignition temperature [K].
T_{LN}	Lower nozzle combustion product temperature [K].
T_r	Reactant temperature [K].
t_r	Cross fractal grid bar width ratio [–].
t	Time [s].
U	Flow velocity [$m\,s^{-1}$].
$\overline{U}$	Mean unconditional axial velocity [$m\,s^{-1}$].
$\overline{U_{...}}$	Mean conditional axial velocity [$m\,s^{-1}$].
u	Axial velocity component [$m\,s^{-1}$].
$\sqrt{u'^2}$	Unconditional axial velocity fluctuation [$m\,s^{-1}$].
$\sqrt{u'^2_{...}}$	Conditional axial velocity fluctuation [$m\,s^{-1}$].
u_{rms}	Root mean square velocity fluctuation [$m\,s^{-1}$].
$\dot{V}_{...}$	Volumetric flow rate [$m^3\,s^{-1}$].
v	Radial velocity component [$m\,s^{-1}$].

$\sqrt{v'^2}$	Unconditional radial velocity fluctuation [$\mathrm{m\,s^{-1}}$].
$\sqrt{v'^2_{\cdots}}$	Conditional radial velocity fluctuation [$\mathrm{m\,s^{-1}}$].
v_η	Kolmogorov velocity [$\mathrm{m\,s^{-1}}$].
X	Mole fraction [–].
x	Axial coordinate [m].
x_s	Distance from origin of first thermal alteration [m].
y	Radial coordinate [m].

Greek Letters

α	Normalised area [–].
Δ	Difference [–].
$\delta_{\nabla T}$	Thermal thickness [m].
δ_{CH}	Laminar CH profile thickness [m].
δ_f	Laminar fuel consumption layer thickness [m].
ε	Rate of dissipation [$\mathrm{m^2\,s^{-3}}$].
Λ	Threshold value [–].
λ_B	Batchelor scale [m].
λ_D	Mean scalar dissipation layer thickness [m].
λ_{MF}	Multi–fluid spatial resolution [m].
λ_{PIV}	PIV spatial resolution [m].
μ	Molecular viscosity [$\mathrm{kg\,m^{-1}\,s}$].
ν_r	Reactants kinematic viscosity [$\mathrm{m^2\,s^{-1}}$].
Φ	Equivalence ratio [–].
ρ_p	Solid Al_2O_3 particle density [$\mathrm{kg\,m^{-3}}$].
τ_b	Convective timescale [s].
τ_c	Chemical timescale [s].
τ_η	Kolmogorov timescale [s].
Θ	Number of thresholds [–].
θ	Individual threshold [–].
τ_{ign}	Auto–ignition delay time [s].
τ_I	Integral timescale of turbulence [s].
τ_p	Particle relaxation time [s].
ξ	Filter width [pixels].

Sub/super-scripts

0	Alignment at the origin; Initial value.
Φ	Dependency on equivalence ratio.
‡	Reference value.
BTB	Back–to–burnt configuration.
b	Bulk flow motion.
FS	Fluid state.
I	Integral scale; Turbulent.
i, j	Pixel index.
k	Velocity component.
LN	Lower nozzle.
max	Maximum.
mix	Mixing fluid.
n	Instantaneous image.
pix	CCD chip pixel.

OH	OH–PLIF signal.
p	Product fluid; Peak value.
q	Extinction conditions.
r	Reactant fluid.
str	Strongly reacting (flamelet) fluid.
T	Total.
$Twin$	Twin flame configuration.
UN	Upper nozzle.
$weak$	Weakly reacting fluid.

1. Introduction

The classification of combustion regime boundaries by means of flow and chemical reaction time and length scales ratios includes the Klimov-Williams criterion [1], where the laminar flame thickness is equal to the Kolmogorov length scale (L_η), resulting in a Karlovitz (Ka) number of unity. The use of more complete combustion regime diagrams has been discussed by Williams [2] and further explored by Borghi [3] and Peters [4] with alternative classifications proposed by Abdel-Gayed et al. [5] and Poinsot et al. [6]. Subsequently, Peters [7] revisited the location of combustion regime boundaries, which are influenced by the impact of heat release on scaling parameters coupled with the inherent multiple chemical timescales (τ_c) within a flame structure or, more generally, a chemically reacting flow.

Practical combustion devices increasingly operate under conditions where turbulent flow can be expected to influence the preheat and reaction layers of flames. Accordingly, the flamelet theory, which has been successfully applied in conventional engines (e.g. via the Bray–Moss–Libby (BML) model [8]), gradually becomes inapplicable [9]. Novel low-polluting combustion technologies that operate in the absence of distinct flame fronts can be expected to experience significant reaction zone broadening e.g. via flameless combustion modes [10]. Related combustion regime transitions in lean ($\Phi = 0.0$, 0.2, 0.4, 0.6 and 0.8) premixed JP-10 (exotetrahydrodicyclopentadiene) flames have been studied by Goh et al. [11] using a back-to-burnt (BTB) opposed jet configuration and comparisons made with the approach to extinction of conventional flames in the corresponding twin flame geometry [12]. Relevant conditions can also be achieved in vitiated jet flames and reaction zone broadening within a shear layer of premixed CH_4/air flames at varying stoichiom-

etry and jet velocity was investigated by Duwig et al. [13]. The study concluded that lean ($\Phi = 0.4$, 0.8) flameless oxidation, e.g. in gas turbines [14], exhibits different turbulence–chemistry interactions compared to fuel–rich ($\Phi = 6.0$) moderate or intense low-oxygen dilution (MILD) combustion used in furnaces. Zhou et al. [15–18] investigated premixed CH_4 flames with thin and distributed reaction zones analysed via simultaneous $CH/CH_2O/OH$, $HCO/CH_2O/OH$ and $temperature/CH_2O/OH$ measurements. A thickening of the CH layer was observed with increasing Ka along with a deeper penetration of CH and HCO into the OH layer. By contrast, Skiba et al. [19] and Wabel et al. [20, 21] did not observe any substantial broadening of the heat release layer for lean ($\Phi = 0.65$ and 0.75) and close-to stoichiometric ($\Phi = 1.05$) methane/air flames using the Michigan Hi-Pilot burner. However, significant broadening of the preheat layer was observed and it was suggested that the elevated viscosity attenuates the turbulence. Minamoto et al. [22, 23] performed direct numerical simulation (DNS) studies using a 16–species skeletal CH_4 mechanism to investigate turbulence–chemistry interactions at varying Damköhler (Da) numbers covering conventional premixed flames and MILD combustion. The reaction zone structure showed significant broadening and a non-bimodal behaviour as well as the existence of interacting thin flamelets at low Da numbers. Lapointe et al. [24] performed DNS of lean ($\Phi = 0.9$) premixed n-heptane flames at high Karlovitz number and attributed the moderate widening of the reaction zone to reduced temperature gradients. The transition to distributed reaction zones of piloted jet flames was also investigated by Skiba et al. [25] for a wide range of turbulent Reynolds numbers (Re_t) and $Da > 1$ and the need for extending conventional combustion regime diagrams was identified.

Turbulent combustion at low Da numbers was investigated by Mas-

torakos et al. [26] by stabilising ultra-lean premixed CH_4 flames against hot combustion products in an opposed jet geometry. Extinction was not observed for hot product stream temperatures > 1550 K and no significant impact of the residual product oxygen fraction was found. The stability of lean premixed CH_4 flames was further characterised by Goh [27] in the range 1520 – 1820 K and Coriton et al. [28] investigated the impact of the composition of the supporting hot combustion products. It was found that lean combustion products favour the reaction support compared to stoichiometric combustion products or a hot inert gas stream. In a related study, Coriton et al. [29] used stoichiometric combustion products to support premixed methane/air flames at varying equivalence ratios. Overall, the opposed jet geometry has significant advantages for a systematic investigation of combustion regime transitions: (i) Relatively well developed turbulence [30, 31]; (ii) Excellent optical access [30, 32]; (iii) Accurate control of boundary conditions [33]; (iv) Aerodynamic flame stabilisation with combustion dynamics related to the intrinsic aerothermochemistry [34]; (v) Individual control of variables affecting the chemical and turbulent timescales (τ_I) [27] and (vi) a compact domain. The turbulence to bulk strain ratio of the opposed jet can also be substantially increased without bulk flow instabilities [33] via cross fractal grids (CFGs) [30, 35, 36] and Goh et al. [34] illustrated the resulting multi-scale character of the turbulence by means of conditional proper orthogonal decomposition. The BTB opposed jet configuration is used here to investigate combustion regime transitions for lean premixed dimethyl ether (DME) flames. The choice of DME is based on the potential relevance as an alternative fuel [37, 38] and the availability of related studies e.g. [39–43].

Combustion regime transitions from topological, e.g. flamelet supported, flames to distributed reaction zones can be expected to be related to the Da

number. Such transitions can accordingly be achieved either by augmenting the turbulence intensity (reducing τ_I) or by slowing down the combustion chemistry (increasing τ_c). For example, Zhou et al. [16] identified the transition to distributed reactions in stoichiometric vitiated CH_4 jet flames for $Re_t > 240$, which reduces to $Re_t > 130$ for $\Phi = 0.4$. In the present study, the Damköhler number is varied in the range from 0.08 to 5.6 by altering τ_c via the stoichiometry ($0.20 < \Phi < 1.0$) while maintaining τ_I constant with $Re_t > 370$ ($Re \simeq 18{,}400$). Based on conventional combustion regime diagrams [4, 7], the current conditions cover transitions from (close to) corrugated flamelets to distributed reaction zones. Hampp and Lindstedt [44] found that self-sustained flames ($Da > 1$) in the current BTB geometry anchored in low compressive strain regions detached from the stagnation plane. By contrast, flames at lower Da numbers stabilised in the proximity of the stagnation plane and were characterised by high strain and vorticity levels.

The multi–fluid approach of Spalding [45] can be used to quantify the evolution of the statistical distribution of intermediate fluid states as a function of the Da number. The application of simultaneous Mie scattering, particle image velocimetry (PIV) and hydroxyl planar laser induced fluorescence (OH-PLIF) permits the identification of five different fluid states (reactants, products, mixing fluid and fluids with high and low reactivity) [46]. The current work accordingly delineates (i) the evolution of the probability distribution between the different fluid states as a function of the Damköhler number including (ii) the flow direction across fluid interfaces and OH gradients and provides (iii) mean flow field statistics, (iv) conditional velocity statistics and (v) a tentative combustion regime classification. (vi) The sensitivity of the distribution between the fluid states to the applied delimiters and (vii) the limitations of bimodal descriptions are evaluated.

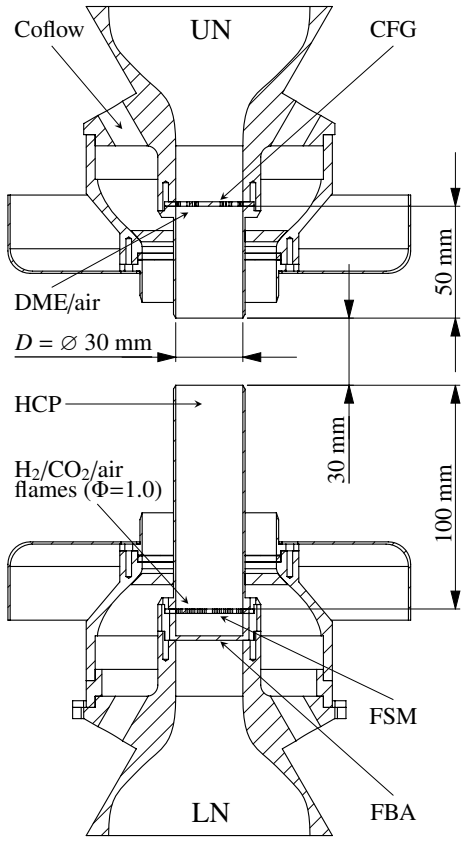

Figure 1: Schematic of experimental configuration. Unreacted premixed DME/air is introduced in the upper nozzle (UN) stabilised by hot combustion products (HCP) from a stoichiometric H_2/CO_2/air flame in the lower nozzle (LN). CFG – Cross Fractal Grid, FBA – Flash Back Arrestor, FSM – Flame Stabilising Mesh.

2. Experimental Configuration

2.1. Burner Configuration

The opposed jet configuration, shown in Fig. 1, was originally developed by Geyer et al. [32] and Geipel et al. [30] and is a direct advancement of the burner used by Goh and co-workers [11, 12]. Flames in opposed jet geometries can suffer from low frequency instabilities as mentioned by Geipel et al. [30] and Coppola and Gomez [47]. The current configuration is free

from such issues as thoroughly analysed by Goh et al. [33]. The geometrical changes introduced in the current work include the substitution of the perforated plate within the lower nozzle (LN) with a fine aperture stainless steel mesh for flame stabilisation (FSM) located 100 mm upstream of the nozzle exit. The LN was further elongated from 50 to 100 mm and the FSM optimised to preclude any flame instabilities and noise generation. The ideal FSM exhibits a blockage ratio of 62 %, an aperture of 0.40 mm (40 mesh) and a wire thickness of 0.25 mm. A second, finer mesh acting as a flashback arrestor (FBA) was installed 12 mm upstream of the FSM.

Reactants were provided using two separate gas mixing systems. Dry and filtered air from Howden compressors and other reactants were supplied at a pressure of 4.0 bar(g). The purities of the cylinder gases were: DME (99.9 %), H_2 (99 %) and CO_2 (99 %). Gases were metered via digital Bronkhorst mass flow controllers featuring a flow uncertainty < 0.8 % [30] and operated using a purpose written LabView interface. Co-flow velocities were regulated using calibrated rotameters set to 30 % of the upper nozzle (UN) exit velocity [30].

2.2. Flow Conditions

The burner was operated in a BTB mode with premixed DME/air injected through the upper nozzle and stabilised by hot combustion products (HCP) from the lower nozzle. The conditions are summarised in Table 1.

2.2.1. Upper Nozzle Conditions

The CFG, installed 50 mm upstream of the UN exit, featured a blockage ratio of 65 % with maximum and minimum bar widths of 2.0 mm and 0.50 mm ($t_r = 4$) [30]. Premixed DME-air mixtures with equivalence ratios

Table 1: Experimental Conditions. FBA – Flash Back Arrestor, FSM – Flame Stabilising Mesh; Dil. – Dilution; NL – Nozzle Length; [1]Cross Fractal Grid (CFG), Blockage ratio 65 %, $t_r = 4$; [2]Based on the viscosity for air – see Table 3 for DME/air mixtures.

UN Conditions Unburnt Reactants		LN Conditions Hot Combustion Products	
$\dot{V}_{UN}$	7.07×10^{-3} m^3 s^{-1} (293 K)	$\dot{V}_{LN}$	3.10×10^{-3} m^3 s^{-1} (293 K)
$U_{b,UN}$	11.0 m s^{-1} (320 K)	$U_{b,LN}$	24.0 m s^{-1} (1700 K)
Fuel	DME	Fuel	H_2
Φ_{UN}	0.0 – 1.0	Φ_{LN}	1.0
T_r	320 K	T_{LN}	1700 K
Grid	CFG[1]	Grid	FBA and FSM
NL	50 mm	NL	100 mm
Re	$> 18{,}400$[2]	Dil.	22 % by volume of CO_2
Re_t	> 370[2]		

$\Phi = (0.0)$, 0.20, 0.40, 0.60, 0.80, 1.0 were injected at a constant volumetric flow rate ($\dot{V}_{UN} \simeq 7.07 \times 10^{-3}$ m^3 s^{-1} at STP). Reactants were preheated to 320 K (T_r) to avoid condensation in comparative ethanol flame studies [48] leading to a nozzle exit velocity of $U_b \approx 11.0$ m s^{-1}. The nozzle separation (H) was set to one nozzle diameter D (= 30.0 mm) yielding a bulk strain rate of $a_b = 2 \cdot U_b/H \approx 750$ s^{-1}. The resulting $Re \simeq 18{,}400$ with $Re_t > 370$ based on an integral length scale of turbulence ($L_I = 4.1$ mm), velocity fluctuations ($u_{rms} = 1.58$ m s^{-1}), measured using hot wire anemometry and PIV, and a kinematic viscosity ($\nu_r = 17.9 \times 10^{-6}$ m^2 s^{-1}) for air at 320 K. Scale information and turbulence spectra obtained with both techniques in fractal grid turbulence have been compared by Geipel et al. [30].

2.2.2. Lower Nozzle Conditions

Highly diluted stoichiometric H_2/air flames were used to provide stable flame anchoring on the FSM with the nozzle exit temperature (T_{LN}) controlled using a CO_2 dilution of 22 % by volume. The temperature was measured using a type R thermocouple indicating heat losses around 10 % to

the burner assembly resulting in $T_{LN} = 1700 \pm 3.5$ K with a maximum peak-to-peak variation of around 15 K (i.e. < 1.0 %). The nozzle jet momenta were matched to locate the stagnation plane in the proximity of the burner centre. This required a volumetric flow rate of $\dot{V}_{LN} = 3.10 \times 10^{-3}$ m^3 s^{-1} (at STP) leading to a burnt gas velocity of $\sim$24 m s^{-1} at the nozzle exit.

2.3. Measurement Setup, PIV and Image Preparation

Simultaneous Mie scattering, OH-PLIF and PIV (5 Hz repetition rate) was carried out using the planar cavity stimulated Raman scattering technique of Kerl et al. [49]. A barium nitrate ($Ba(NO_3)_2$) crystal was pumped with the first of the double pulsed Litron Nano LG 175-10 Nd:YAG PIV laser at 532 nm, producing a Raman shift of 1047 cm^{-1} [50]. Subsequent spatial separation of the pump and first Stokes (563.4 nm) beam and frequency doubling of the latter using a barium borate ($Ba(BO_2)_2$) crystal allows OH excitation at 281.7 nm via the $R_2(5)$ line. The Mie scattering (first pulse) and PIV measurements were performed using the 2^{nd} harmonic of the same light source. The overlaid light sheets (281.7 nm and 532 nm) featured a height of $1D$ and thicknesses < 0.50 mm and < 0.25 mm, respectively. Pulse energies were around 2 mJ at 281.7 nm and 30 mJ at 532 nm with a pulse width of 4.0 ns. Two interline-transfer CCD-cameras (LaVision Imager Intense) were used with one connected to an intensified relay optics unit to record the OH signal. An optical beam splitter with a transmissivity around 97 % at 532 nm and a reflectivity > 97 % from 300 – 320 nm separated the particle Mie scattering from the OH-PLIF signal. The OH fluorescence was recorded using a 105 mm ultraviolet lens (f/2.8) from LaVision, equipped with a bandpass filter featuring a transmissivity of $< 1 \times 10^{-5}$ at 532 nm and > 85 % from 300 – 320 nm. A Tokina AF 100 mm lens (f/2.8),

equipped with a 3 nm bandpass filter at 532 nm to minimise noise (e.g. from CH-chemiluminescence), was used for the PIV measurements. The PIV laser pulses were separated by 25 µs to minimise spurious vectors.

Each air stream was seeded separately using aluminium oxide (Al_2O_3) powder ($\rho_p = 3900\ \mathrm{kg\,m^{-3}}$, $d_{p,50} = 0.44$ µm and $d_{p,90} = 1.7$ µm). The particle relaxation time (τ_p) [51] for the UN was estimated for $d_{p,90}$ ($d_{p,50}$) resulting in $\tau_p \approx 30$ µs (2 µs). A viscosity $\mu = 60.4 \times 10^{-6}\ \mathrm{kg\,m^{-1}\,s^{-1}}$ was obtained for the lower nozzle HCP at chemical equilibrium resulting in a particle relaxation time of 10 µs (0.71 µs). Following Han and Mungal [52], the smallest PIV timescales were estimated to 65 µs and 30 µs for the UN and LN respectively. The Stokes number was below 0.1 for 90 % ($d_{p,90}$) of seeding particles based on the estimated Kolmogorov timescale ($\tau_\eta \simeq 300$ µs) in the reactants. The estimated frequency response (3.9 kHz) of the $d_{p,50}$ particles [53] was above the highest turbulent fluctuations (3.3 kHz) associated with the Kolmogorov timescale in the reactants. The use of small tracer particles can result in peak locking [54] and bias the velocity vector determinations. The peak locking criteria was maintained < 0.05 and therefore well below the recommended upper limit of 0.1 [55].

2.3.1. Particle Image Velocimetry

Cross-correlation PIV (LaVision Davis 8.1) was performed using adaptive interrogation regions of decreasing size (128 × 128 to 48 × 48 with a 75 % overlap) as it offers the highest accuracy, spatial resolution and robustness at the penalty of significantly increased calculation time [56]. The final pass of the smallest interrogation region (IR) was performed on a high accuracy mode with the adaptive PIV calculation warping the round weighted window to an elliptical (maximum aspect ratio of four) Gaussian bell to

incorporate the local flow field acceleration. The resulting velocity field consists of 115 × 88 vectors with a spacing of 300 µm. No spatial smoothing was applied. The adaptive shape modulation reduces the nominal IR size in the direction of steep velocity gradients and thereby improves the spatial resolution by up to a factor of two compared to conventional IRs [56, 57]. Hence, the lower limit spatial resolution was estimated as $\lambda_{PIV} \simeq (x_{pix} \cdot 48)$ / $(M \cdot 2)$ = 595 µm, where $M = 0.26$ is the optical magnification and x_{pix} = 6.45 µm the pixel size. The value is close to an order of magnitude below the integral length scale of turbulence. The dynamic velocity and spatial range [58] was estimated to 194 and 87, respectively.

The IRs of the adaptive PIV incorporate the local velocity gradient with the potential to minimise the in-plane loss of particles and thus the gradient bias [59]. The out-of-pattern effect of large particle displacements is minimised by means of a multi-pass window shifting technique [60]. Uncertainties emerging from thermal gradients include thermophoresis leading to velocity lag [61]. The maximum temperature gradient of 1.6×10^6 K m^{-1} in a laminar stoichiometric DME/air flame suggests a thermophoretic velocity of -0.11 m s^{-1} $\simeq$ 1 % of the UN bulk velocity. Beam steering effects [62] were estimated based on the same laminar flame with a maximum observed flame diameter of 200 mm and a thermal flame thickness $\delta_{\nabla T} = 0.37$ mm. This provides a conservative estimate for beam steering of 15 µm (i.e. ∼5 % of the PIV laser light sheet thickness) at the far end of the interrogation region. The movement of the flame between the PIV pulses is negligible as τ_η is an order of magnitude bigger than Δt. The overall uncertainty due to random errors in the PIV calculations was estimated based on correlation statistics [63]. The maximum uncertainty of the velocity magnitude was determined to 0.3 m s^{-1} or $<$ 3 % of the UN bulk velocity. The impact of 3D

effects was discussed by Hampp and Lindstedt [44].

2.3.2. Image Pre–Processing

The number of images was increased from 1000 [33] to 3000 [44] in order to improve the statistical accuracy for comparatively rare events. Statistical independence of realisations is essential in the current work and, accordingly, a minimum temporal separation of the order of τ_I is required. Image pre-processing (i.e. alignment, data reduction and noise reduction) was performed prior to the application of the multi–fluid detection algorithms. Mie scattering operations were conducted on the first of the double frame images. The physical misalignment ($\sim$100 µm) of the OH-PLIF and Mie scattering images was corrected by superimposing the coordinate systems via calibration images. For data reduction, the OH and Mie images were truncated to $15.0 < x < 15.0$ and $-11.6 < y < 14.1$ mm, resolved by 829×709 and 1193×1020 pixels, respectively. The spatial extent of the Mie images for the stoichiometric case was smaller due to a change in camera setup (i.e. $-10.1 < x < 10.1$ and $-13.4 < y < 14.4$ mm resolved by 711×980 pixels). The coordinate system convention is shown in Fig. 2 with the reference windows close to the nozzle exits used to define reference signals.

The impact of extraordinarily strong Mie scatterers was dampened in order to avoid biasing of the smoothing operations of the density segregation algorithm using an universal outlier technique [64] and a filter width of $\xi = 16$ pixels. Removal of noise from the instantaneous OH images was achieved by a four-level Haar [65] wavelet decomposition. Pre-determined thresholds were used to subtract noise from the segregated images, which were then reconstructed to obtain a clean OH signal. Inhomogeneities in the laser beam

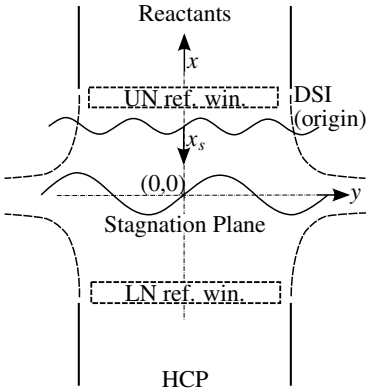

Figure 2: Coordinate system convention. UN – upper nozzle; LN – lower nozzle; ref. win. – reference window; HCP – hot combustion products, DSI – density segregation iso–contour; x_s – Axial coordinate aligned at DSI.

profile can cause spurious signal gradients. An average laser beam profile was recorded using the OH intensity of the matching HCP stream and used for normalisation. In order to account for pulse-to-pulse intensity fluctuations the normalisation profile was weighted and iteratively optimised. The ideal weighting factor successfully removed spurious axial signal gradients in the proximity of the LN exit. Images were only accepted for further processing if the determined weighting factor was found constant between iterations (rejection rate < 1 %).

3. Chemical Timescales and Limiting Conditions

Chemical timescales and flame properties were determined computationally to support the analysis of experimental data in terms of non-dimensional groups (e.g. Damköhler numbers). The DME mechanism of Park [66], featuring the QRRK based decomposition rate of Fischer et al. [40] with abstraction rates from the same study (H, OH, CH_3) and Curran et al. [67] (O, O_2, HO_2), was used in combination with the hydrogen chemistry of Burke

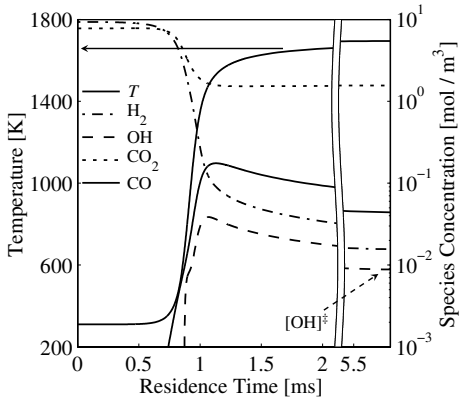

Figure 3: Laminar flame replicating the experimental LN conditions, e.g. reactant flow rates, temperature and residence time, to provide a value for the reference OH concentration $[\mathrm{OH}]^‡$ and boundary conditions for the BTB opposed jet calculations.

et al. [68]. The mechanism was validated against laminar burning velocities (e.g. [39, 69, 70]) and species profiles [71, 72] with good agreement.

3.1. Lower Nozzle Combustion Products

The hot combustion products, see Sec. 2.2.2, emerge from the lower nozzle in close to chemical equilibrium. The intensity of OH (I) is clearly detectable in the experimental OH–PLIF images with a signal-to-noise (SNR = mean / rms) ratio of 3.5 within the HCP stream. The thermochemical state at the nozzle exit can also be estimated using laminar flame calculations, see Fig. 3, replicating the experimental conditions (e.g. reactant flow rates and residence time). The measured OH intensity ($I^‡$) and the corresponding computed concentration ($[\mathrm{OH}]^‡ \approx 8.82 \times 10^{-3}$ mol/m^3) at the LN exit provide well defined experimental and computational reference values.

3.2. Stagnation Plane Mixing Layer

Turbulent transport across the stagnation plane leads to mixing of the HCP and the UN stream. A mixing layer OH surplus ($I/I^‡ > 1$) was found

experimentally for the isothermal case ($\Phi = 0.0$) as shown in Fig. 4. The shaded area illustrates the normalised intensity PDF ($0 < I/I^{\ddagger} < \infty$). While the mean signal suggests a near monotonic decline towards the stagnation plane, the PDF indicates pockets of excess OH in particular in the proximity of the stagnation plane ($x/L_I = 0$). The upper limit, defined as containing 95 % of all samples, corresponds to a normalised signal intensity $I/I^{\ddagger} \leq 1.8$ located at $x/L_I \approx$ -1/2.

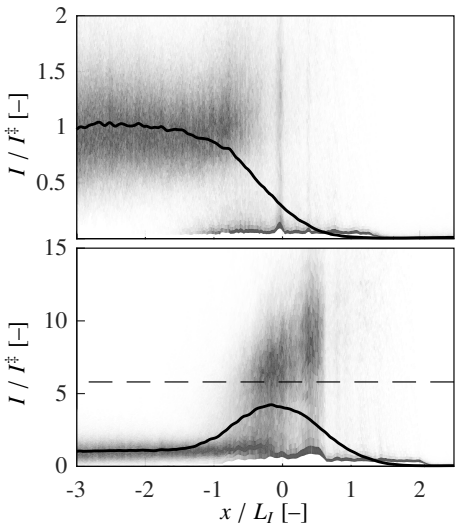

Figure 4: Experimentally observed (normalised) OH signal intensities along the stagnation point streamline in the BTB configuration. Top: The isothermal case with $\Phi = 0.0$. The solid curve shows the mean and the shaded area the PDF for $0 < I/I^{\ddagger} < \infty$. Bottom: The corresponding case with $\Phi = 1.0$ with the dashed line indicating the estimated intensity ratio at the twin flame extinction point (see Sec. 3.4).

The cause can readily be analysed by considering the mixing of HCP with air by means of perfectly stirred reactor calculations covering mixing times from the Kolmogorov (τ_η, see Sec. 5.6) to the integral (τ_I) timescale. The initial temperature (T_0) follows from the blending fraction between the two streams and takes into account changes in the heat capacity. The increased

concentration ($[OH]/[OH]^{\ddagger} > 1$), shown in Fig. 5, stems from residual chemical reaction at low air blending fractions ($T_0 \geq 1400$ K). The maximum surplus $[OH]/[OH]^{\ddagger} \simeq 1.85$ occurs at short mixing times at $T_0 \simeq 1570$ K and is consistent with the experimental data shown in Fig. 4. The OH signal is quenched at higher air blending ratios and vanishes around 1000 K.

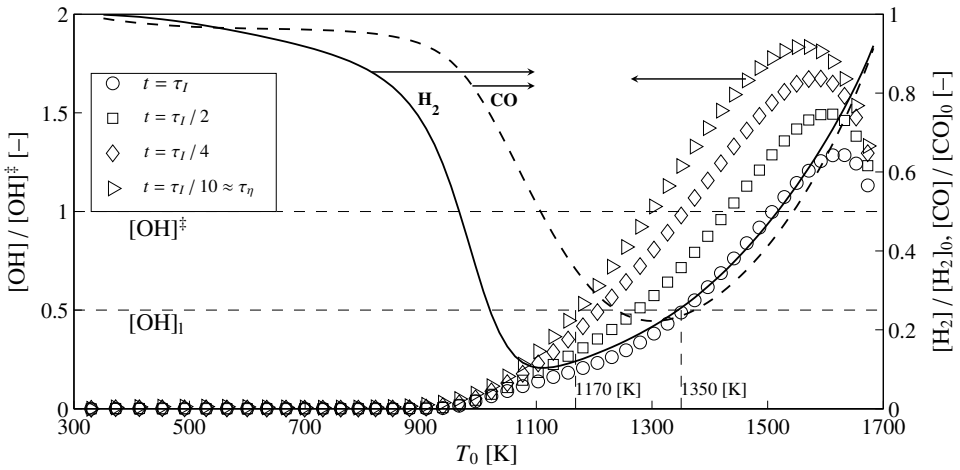

Figure 5: OH concentration following mixing of cold air with HCP to establish the maximum OH signal level in the absence of DME using perfectly stirred reactor calculations. Symbols show the normalised OH concentration for residence times from the integral timescale (τ_I) to the Kolmogorov timescale (τ_η). Also drawn is the lower OH detection limit $[OH]_l$ and the reference signal intensity $[OH]^{\ddagger}$. Further shown is the consumption of residual H_2 (CO) – solid (dashed) line – of the HCP due to the admixture of cold air at $t = \tau_I/4$ normalised by their initial concentrations.

3.3. Auto-ignition in Mixing Pockets

The turbulent transport of HCP fluid across the stagnation plane results in preheating (and dilution) of the reactants and may lead to auto-ignition. Consequently, the auto-ignition delay times (τ_{ign}) for DME/air mixtures (see Fig. 6 and Table 3) were determined using shock tube calculations. The values suggest that a residence time of τ_I corresponds to an auto-ignition temperature $T_{ign} \approx 1196 \pm 10$ K that is relatively independent on Φ.

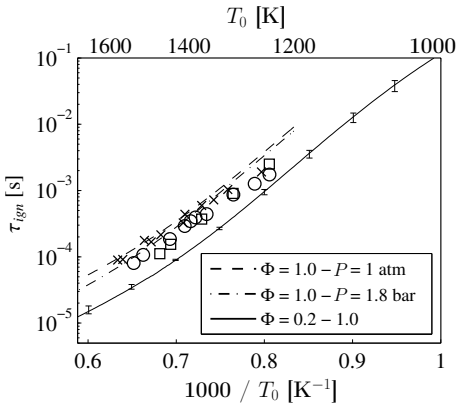

Figure 6: Validation calculations at $\Phi = 1.0$ compared at $P = 1.0$ atm and 1.8 bar with experimental auto–ignition delay times (□ – [73] $\Phi = 1.0$, $P = 1.8$ atm; ◯ – [74] $\Phi = 1.0$, $P = 1.0$ bar; × – [75] $\Phi = 1.0$, $P = 1.2$ atm) for 1 % DME in O_2/Ar mixtures. Also shown is the average auto–ignition delay time for the cases investigated, i.e. DME-air, with the error bar representing the variation with $\Phi = 0.20 - 1.0$ ($P = 1$ atm).

3.4. Strained Laminar Flame Extinction Points

The frequency of local extinction increases with decreasing Damköhler number while global extinction is prevented in the BTB configuration by the external enthalpy source [11, 29]. At low Da numbers, the strain acting on the reaction onset iso-contour exceeds the extinction strain [44]. By contrast, self-sustained flames at higher Da numbers detach from the stagnation plane, as also observed by Coriton et al. [29], and are subject to conventional extinction criteria. The extinction points were accordingly determined by means of strained laminar counterflow calculations [76] performed for twin flame ($\Phi \geq 0.60$) and BTB configurations. The computational domain was resolved by 390 distributed cells providing a resolution of the CH peak of < 12 µm (i.e. > 25 cells) due to local refinement as exemplified in Fig. 7. The accuracy of predicted extinction points was assessed by comparing with experimental data from Wang et al. [39] and, for example, a computed ex-

Table 2: Extinction point conditions for premixed DME/air twin flames. The $[OH]_q/[OH]^{\ddagger}$ ratio and $[CH]_q$ were obtained at the twin flame extinction point and $[OH]_{BTB}/[OH]^{\ddagger}$ and $[CH]_{BTB}$ in the BTB geometry at the corresponding integrated heat release rate.

Φ	–	0.60	0.80	1.0
a_q	s^{-1}	600	2000	3100
T_q	K	1555	1683	1760
$[OH]_q/[OH]^{\ddagger}$	–	3.5	5.5	5.8
$[OH]_{BTB}/[OH]^{\ddagger}$	–	3.4	5.2	5.6
$[CH]_q \times 10^8$	mol m^{-3}	0.08	0.55	1.48
$[CH]_{BTB} \times 10^8$	mol m^{-3}	0.10	0.60	1.37

tinction point for a DME/air flame ($\Phi = 0.80$) stabilised against N_2 was $\approx$ 510 s^{-1} compared to the measured value of $\approx$ 500 s^{-1}.

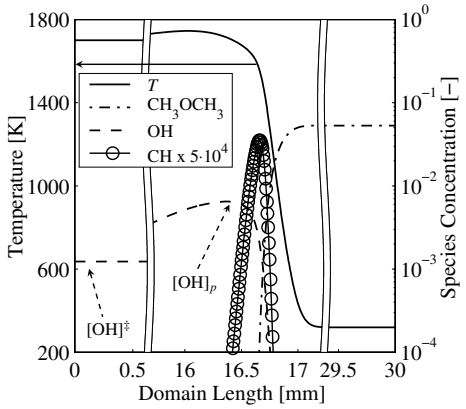

Figure 7: Laminar opposed jet flame in the back-to-burnt configuration at $a = 825$ [s^{-1}] and $\Phi = 0.80$. The lower nozzle exit is located at domain length = 0 mm and the upper nozzle at 30 mm. The symbols on the CH profile exemplify the spatial resolution of the laminar BTB calculation. The x-axes are broken to enhance the readability.

The twin flame extinction points are summarised in Table 2. The corresponding integrated heat release rate ($\int \dot{Q}_q$) provides the critical (minimum) value required for self–sustained burning. The correlation of $\int \dot{Q}_q$ with the peak temperature and peak concentrations of selected species (i.e. $[OH]_p$, $[CH]_p$, $[CH_2O]_p$, $[H_2]_p$ and $[CO]_p$) is shown in Fig. 8. The twin flame ther-

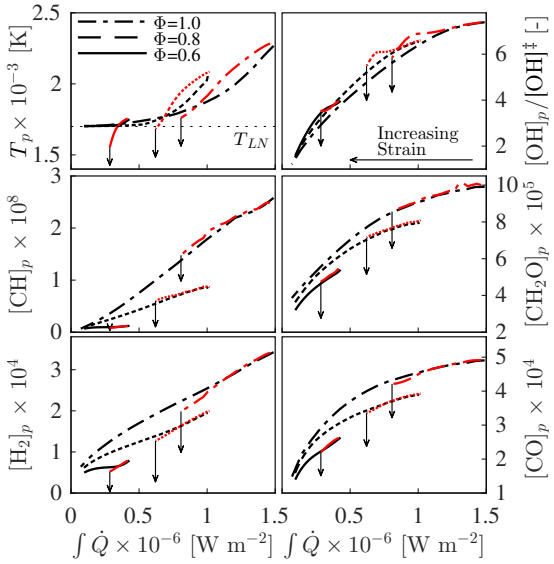

Figure 8: Correlation between integrated heat release rate($\int \dot{Q}$), peak temperature (T_p) and peak radical ($[\mathrm{OH}]_p$, $[\mathrm{CH}]_p$, $[\mathrm{CH_2O}]_p$, $[\mathrm{H_2}]_p$ and $[\mathrm{CO}]_p$) concentrations in [mol/m^3]. The $[\mathrm{OH}]_p$ values are normalised by the HCP equilibrium OH concentration ($[\mathrm{OH}]^{\ddagger}$). The black lines correspond to the BTB and the red (grey) lines represent the twin configuration.

mochemical state correlates well with the corresponding BTB state at the same rate of heat release ($\int \dot{Q}_{BTB} = \int \dot{Q}_{Twin}$). Accordingly, BTB flames with $\int \dot{Q}_{BTB} < \int \dot{Q}_q$ rely on thermal support for sustained chemical activity with, for example, the OH peak concentration at extinction approximately marking the minimum value consistent with self-sustained burning in both configurations as shown in Table 2.

3.5. Flame Parameters and Dimensionless Groups

The Re_t and conventional Damköhler number (Da), see Eq. (1), are commonly used to classify combustion processes.

$$\tau_I = \frac{L_I}{u_{rms}} \qquad \tau_c = \frac{\delta_f}{S_L} \qquad Da = \frac{\tau_I}{\tau_c} \tag{1}$$

The integral timescale of turbulence (τ_I) was based on the measured u_{rms} and L_I. The chemical timescale (τ_c) was obtained from the calculated laminar flame thickness (δ_f) based on the 5 – 95 % fuel consumption layer (i.e. the inner layer thickness of Peters [77]) and the laminar burning velocity (S_L). The resulting values are compared to the 5 – 95 % CH peak (δ_{CH}) width [78] and the thermal thickness $\delta_{\nabla T} = (T_b - T_u)/max(\nabla(T))$ [79, 80] at different rates of strain in Fig. 9. For all cases the maximum differences are less than 30 % for $a > a_b = 750$ s^{-1}. The values of δ_{CH} are strongly dependent on the rate of strain for very lean mixtures. For $\Phi \leq 0.40$ the bulk rate of strain significantly exceeds the extinction strain of the corresponding twin flames. Hence, values of δ_f and S_L were obtained in the BTB configuration at a low rate of strain ($\sim$10 % of a_b) for all mixtures to provide a consistent parameter set. Values are also compared with the corresponding twin flames for $\Phi \geq 0.60$ as shown in Table 3.

The resulting range of Damköhler numbers $0.08 < Da < 5.6$ covers the conventional transition ($Da \simeq 1$) to a distributed combustion regime around $\Phi = 0.60$. The range $3.3 \leq u_{rms}/S_L \leq 40$ for $\Phi = 1.0$ – 0.20 includes conditions beyond the intense turbulence regime limit $u_{rms}/S_L \simeq 19$ defined by Driscoll [81]. The current Da number definition and the proposed transition to the intense turbulence regime appear broadly consistent. As the Da is reduced, the ratio of the adiabatic to the initial reactant temperature (T_{ad}/T_r) decreases from 7.2 to 2.8, see Table 3. The lower limit will be further reduced as the reaction onset at low Da requires HCP support [44], which results in an elevated reaction onset temperature and, in combination with the increasing flame thickness, a significant reduction in thermal gradients across reaction zones.

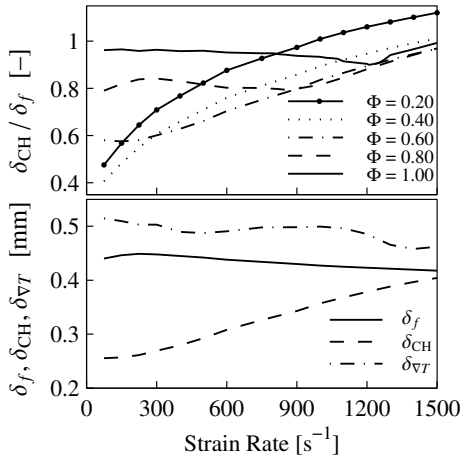

Figure 9: Top: Comparison of the inner layer thickness (δ_f) [77], defined as the 5 – 95 % fuel consumption layer thickness, and the 5 – 95 % CH profile width (δ_{CH}) [78] as a function of strain at varying Φ (top). Bottom: Comparison of the δ_f, δ_{CH} and thermal thickness ($\delta_{\nabla T} = (T_b - T_u)/max(\nabla(T))$) [79, 80] as a function of strain for $\Phi = 0.60$.

4. Multi–Fluid Post–Processing Method

Combustion with low Da can lead to a broadening of reaction zones as observed in vitiated jet flames [15–18, 82] and DNS [22, 83] and a bimodal two–fluid description (reactants and products) with a negligible probability of encountering chemically active states can become problematic [9]. Spalding [45] suggested a multi–fluid approach that permits the identification of intermediate fluid states. The concept is explored here using simultaneous Mie scattering, PIV and OH – PLIF combined with a purpose written algorithm that detects four iso–contours in each instantaneous image pair to distinguish up to five different fluid states.

The methodology combines a density segregation technique [34] with a threshold based on the measured OH intensity that segregates the HCP fluid from regions with elevated OH resulting from the combustion of DME. The

Table 3: Summary of turbulence and chemical parameters used to derive the turbulent Reynolds, Damköhler and Karlovitz numbers for varying Φ at a low strain rate ($a = 75$ s^{-1}) in the BTB and twin flame configuration. The turbulence conditions were evaluated for the reactants ($T_r = 320$ K). The auto–ignition delay time (τ_{ign}), Da_{ign}, Ka_{ign} and Da_b were evaluated at $T_{LN} = 1700$ K.

		BTB / Twin Flame				
Φ	–	0.20	0.40	0.60	0.80	1.0
S_L	m s^{-1}	0.04/—	0.06/—	0.21/0.21	0.39/0.40	0.50/0.50
δ_f	mm	1.31/—	1.07/—	0.44/0.45	0.27/0.26	0.22/0.22
τ_c	ms	30.6/—	17.0/—	2.07/2.14	0.68/0.65	0.44/0.44
τ_{ign}	µs			12.6±0.08		
T_{ad}/T_r	K	2.8	4.3	5.5	6.6	7.2
u_{rms}	m s^{-1}	1.59	1.59	1.59	1.54	1.67
L_I	mm	4.1	4.1	4.1	4.1	4.1
τ_I	ms	2.58	2.58	2.58	2.66	2.46
v_η	m s^{-1}	0.25	0.24	0.23	0.22	0.22
L_η	µm	71	71	73	75	74
τ_η	ms	0.29	0.29	0.31	0.33	0.33
τ_b	ms			8.68		
a_q	s^{-1}	—	—	600	2000	3100
a_T	s^{-1}	4200	4160	3940	3750	3755
ε_r	m^2 s^{-3}	210	200	173	150	151
$\nu_r \times 10^6$	m^2 s^{-1}	17.5	17.2	17.0	16.7	16.5
Re_t	–	373	379	383	378	415
u_{rms}/S_L	–	37.3/—	25.2/—	7.57/7.57	3.88/3.85	3.32/3.32
Da	–	0.08/—	0.15/—	1.24/1.21	3.9/4.1	5.6/5.6
Da_{ign}	–			214 ± 13		
Da_b	–			701 ± 42		
Ka	–	106/—	58.7/—	6.66/6.90	2.05/1.97	1.34/1.34
Ka_{ign}	–			0.046 ± 0.003		

latter can be related to the gas mixing layer interface defined by Coriton et al. [29]. No further delineation was made for mixtures with a strained flame extinction point significantly below the bulk strain (i.e. $\Phi = 0.20$ and 0.40). Flames where the bulk strain ($\simeq 750$ s^{-1}) is similar to the corresponding extinction strain rate can detach from the stagnation plane. Hampp and Lindstedt [44] analysed the rate of strain on material surfaces under such conditions and showed that flamelet burning can occur. The thermochemi-

cal states of BTB and twin flames at the rate of heat release corresponding to the twin flame extinction point are very similar as shown in Sec. 3.4. Accordingly, a threshold based on the OH intensity at extinction was introduced to explore the probability of encountering a burning mode consistent with flamelet combustion. The selected fluid states are:

Reactants: Fresh reactants emerging from the UN that have not undergone any thermal alteration (i.e. no combustion or mixing processes).

Mixing fluid: A fluid state without detectable OH signal that has been exposed to a thermal change (i.e. via mixing with HCP).

Strongly reacting fluid: Regions with a strong OH signal intensity consistent with self-sustained (e.g. flamelet) burning. Conventional aerothermochemistry conditions and extinction criteria apply [84].

Weakly reacting fluid: A fluid state with modest levels of OH, e.g. ultra lean flames sustained by thermal support from an external enthalpy source or combustion products approaching equilibrium.

Hot combustion products: The hot combustion products that emerge from the LN provide a well defined reference state.

Sample images with overlaid PIV vectors and detected iso–contours are shown in Fig. 10 and the overall flow chart used to determine the different fluid states is illustrated in Fig. 11.

4.1. Density Segregation Technique

PIV tracer particle based density segregation (DS) techniques are widely used, e.g. [34, 85, 86], and the current algorithm is a variant that is capable

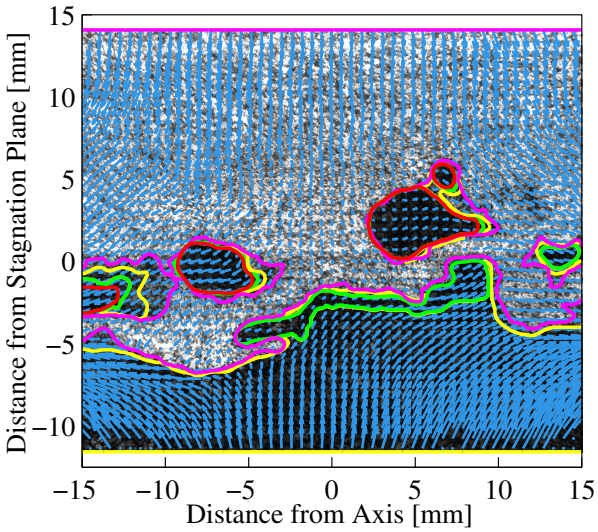

(a)

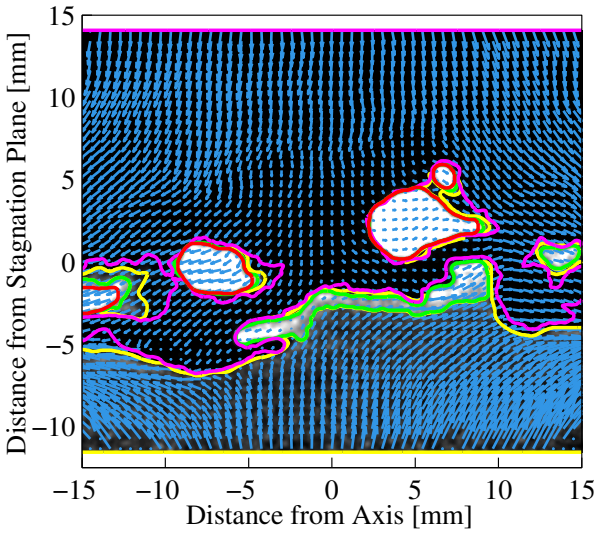

(b)

Figure 10: Identification of multiple fluid states for a DME / air flame at $\Phi = 0.80$: (a) Image showing Mie scattering; (b) Image showing OH-PLIF signal with overlaid PIV vectors. The pink line is the DS iso–contour enclosing the reactant fluid, yellow line encloses the entire OH field, green line encloses the weakly reacting fluid and red line encloses the strongly reacting (e.g. flamelet) fluid. The mixing fluid is bounded by the pink and yellow lines.

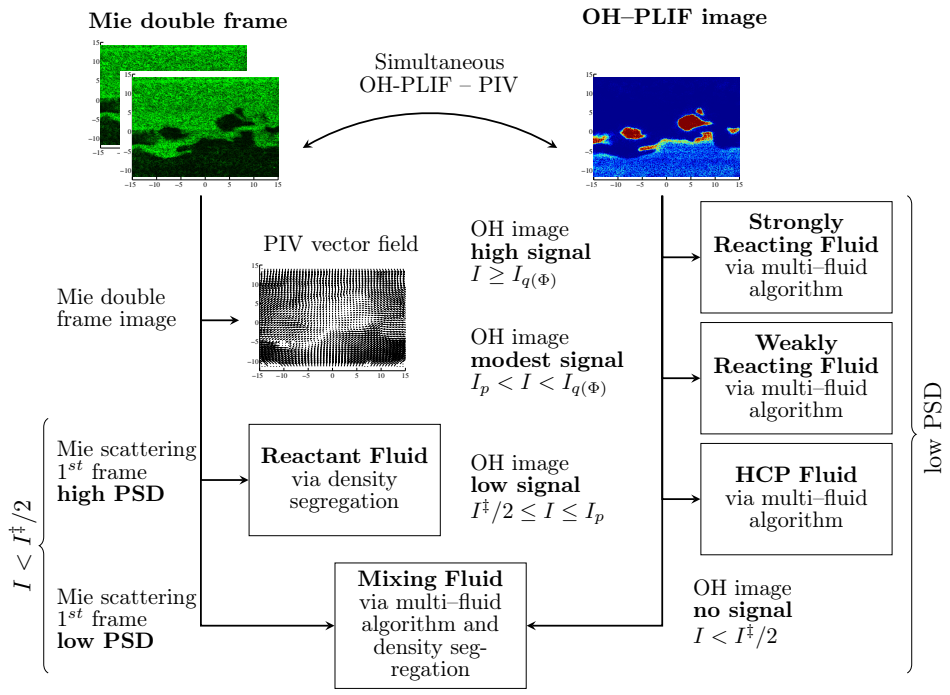

Figure 11: Schematic of the post–processing methodology. PSD – particle seeding density; I – experimental OH–PLIF signal intensity; $I^{\ddagger}$ – reference signal intensity; $I^{\ddagger}/2$ – detection limit; I_p – maximum signal intensity in the absence of UN fuel; $I_{q(\Phi)}$ – minimum signal intensity resulting from self-sustained burning as defined by Eq. (4).

of detecting multiple and fragmented splines [48]. Islands detached from the primary reactant field were required to exceed a minimum size limit (≥ 1.6 mm^2 $\simeq 0.2$ % of the full IR) associated with the applied smoothing filter width to assure unambiguous detection. The DS algorithm detects the first thermal alteration iso–contour of the reactants based on a binary Mie scattering image via Moore-Neighbor tracing with a Jacobs stopping criteria [87]. The average seeding densities of the LN and UN were estimated to $N_{sd,LN} \approx 4 \times 10^{10}$ and $N_{sd,UN} \approx 5 \times 10^{11}$ particles/m^3. A relatively high particle seeding density is beneficial for an accurate detection of the density segregation iso-contour and the PIV calculation in the products. The

present particle seeding density does not alter the thermal conductivity [88] or the heat capacity of the gas noticeably (i.e. $\ll$ 1 %). Changes in the seeding density (N_{sd}) can be induced by chemical reactions or the mixing of reactants with combustion products with a different N_{sd}. An UN to LN seeding density ratio of $N_{sd,UN} \geq 1.75 \cdot N_{sd,LN}$ was found sufficient to ensure an unambiguous determination of the density segregation iso–contour based on a 20 % alteration of the UN reactant seeding density. Images with a lower ratio or over–seeded images were rejected at a rate $<$ 5 %. Seeding density changes due to combustion provide the upper limit of 780 K of the DS iso-contour that is dependent on the adiabatic flame temperature (e.g. T_{ad} = 2300 K for Φ = 1.0) and the smoothing filter width (ξ = 16). The lower limit was estimated to 437±39 K (see Fig. 13 and Sec. 4.2.2).

The accuracy of the DS algorithm was determined via synthetic Mie scattering images obtained from a random particle generator [89]. Density changes were inferred from separately recorded Rayleigh images for flames with Φ = 0.80 (Da = 8.8 and Re_t = 200) and Φ = 0.20 (Da = 0.08 and Re_t = 350). A sample Rayleigh intensity and synthetic Mie scattering image pair is shown in Fig. 12. The particle size distribution matched the experiment, while the overall seeding density was varied randomly within the experimental limits. The particle density segregation algorithm was applied to the synthetic Mie scattering images and the determined iso-contour was compared to the 600 K iso-contour obtained from the Rayleigh thermometry. The latter corresponds to the estimated thermal condition of the Mie scattering iso-contour (see Fig. 13 and Sec. 4.2.2) and also approximately to the Schlieren contour [90]. The average and rms distance between the Rayleigh and DS iso-contour was 86 ± 8 µm and is thus below the thinnest laminar flame thickness (δ_f = 220 µm for Φ = 1.0).

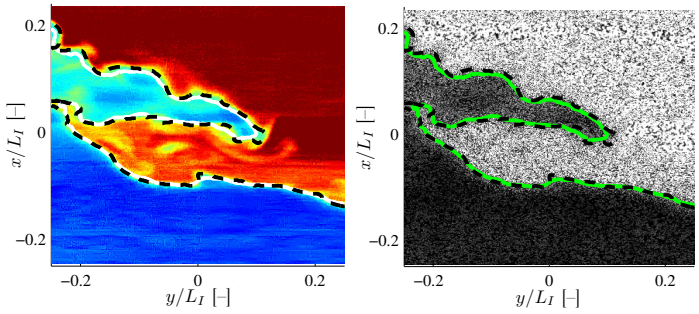

Figure 12: Sample (a) Rayleigh intensity and (b) synthetic Mie scattering image for a DME / air $\Phi = 0.20$ flame at $Re_t = 350$. The dashed black line is the Rayleigh iso-contour and the white or green solid line the DS iso-contour.

4.2. Fluid Detection using OH-PLIF

The experimentally determined OH fluorescence signal intensities were used to segregate the reactive fluid states as outlined above. Alternative methods are possible by using other chemical species (e.g. CH or CH_2O). However, the current procedure has the benefit of simplicity. The OH-PLIF measurements were conducted in the linear regime [91] and the fluorescence power (S_f) to OH mole fraction (X_{OH}) ratio is given by Eq. (2). The overlap integral is nearly temperature independent [92] and was incorporated into the temperature invariant constant C (laser line-width $\simeq 1.5$ cm^{-1}).

$$\frac{S_f}{X_{\mathrm{OH}}} = C \cdot I^{\nu} \cdot k_{v'J'v''J''} \cdot \frac{A_{21}}{A_{21} + Q_{21}}. \tag{2}$$

In Eq. (2), A_{21} is Einstein spontaneous emission coefficient, Q_{21} the collisional quenching rate and I^{ν} the laser irradiance. The temperature dependency of the absorption line strength ($k_{v'J'v''J''}$) of the $R_2(5)$ excitation line was evaluated via LIFBASE v.2.1.1 [93] and the collision quenching cross sections were obtained from Garland and Crosley [94] and Smith and

Crosley [95]. The dependency of the OH collision cross section with CO_2, O_2, and H_2O on temperature is significantly reduced for the temperature range of interest ($T > 1200$ K) [92]. The data was combined with species profiles from a BTB laminar flame (DME/air, $\Phi = 0.80$, $a = 825\ s^{-1}$, see Fig. 7) to estimate the fluorescence yield as a function of temperature. A maximum uncertainty of 10 % was determined for temperatures > 1000 K [48] and a linear correlation, valid over the range $1200 \leq T\ (\mathrm{K}) \leq 2200$, was consequently used to segregate the OH signal into intensity bands. The determined uncertainty is consistent with the findings of Battles and Hanson [92]. The normalised HCP signal intensity ($I^{\ddagger} = 1.0$) is defined at a fixed location (dashed LN rectangle in Fig. 2) and provides the required reference value. Disconnected areas from the primary OH–field were only accepted if $> 0.6\ mm^2$ to ensure an unambiguous detection due to the applied filter width of 4 pixels. All OH signal intensities ($I_{\ldots}$) correspond to experimental data.

4.2.1. Hot Combustion Products

The minimum detectable OH intensity was around $I^{\ddagger}/2$. The maximum signal intensity ratio in the absence of UN fuel was determined in Sec. 3.2 to $I_p/I^{\ddagger} = 1.8$ (containing 95% of all samples) with a corresponding computed value $[\mathrm{OH}]_p/[\mathrm{OH}]^{\ddagger} = 1.85$. The rounded threshold is defined in Eq. (3) and is related to the gas mixing layer interface introduced by Coriton et al. [29].

$$\Lambda_{\mathrm{OH},p} = 2.0 = \lceil \left(\frac{I_p}{I^{\ddagger}} \right) \rceil = \lceil \left(\frac{[\mathrm{OH}]_p}{[\mathrm{OH}]^{\ddagger}} \right) \rceil \tag{3}$$

The defined range for the HCP fluid is thus limited by $1/2 \leq I/I^{\ddagger} \leq 2$ and independent of the reactant stoichiometry. Away from the lower nozzle

exit, the HCP fluid can contain DME combustion products. Higher normalised OH signal intensities ($I/I^{\ddagger}$) consequently stem from the combustion of DME. The threshold $\Lambda_{\mathrm{OH},p}$ corresponds to an estimated OH concentration of 1.76×10^{-2} mol/m^3.

4.2.2. Mixing Fluid

The mixing fluid was defined as regions with a detectable drop in seeding density of the reactant stream (i.e. a thermal alteration of the fluid) and an OH signal intensity below the detection limit (i.e. $I^{\ddagger}/2$). The change in the seeding density (N_{sd}) is a consequence of the mixing of the UN reactant stream (high seeding density) with the HCP. The required blending fraction for an unambiguous detection of the Mie scattering iso-contour was estimated for the UN to LN seeding density ratio range of $1.75 \leq N_{sd,UN}/N_{sd,LN} \leq 10^2$ as shown in Fig. 13. The lower limit follows from the minimum seeding density ratio requirement and the upper limit is set by the ratio of saturation to background signal of the camera. The heat capacity and density of the reactants and HCP were inferred from the laminar flame calculations discussed in Sec. 3. A HCP blending fraction of 3 – 7 % is sufficient to identify the iso-contour, which corresponds to an estimated temperature of 437±39 K assuming inert and adiabatic mixing. The OH detection limit provides an estimate for the upper limiting HCP blending fraction of 50 – 70 %, which corresponds to an approximate thermal contour of 1260±90 K (see Fig. 5). The limits indicate the wide range of conditions of this fluid state and refinements are possible if there is a desire to identify regions of low temperature ignition chemistry (e.g. characterised by CH_2O).

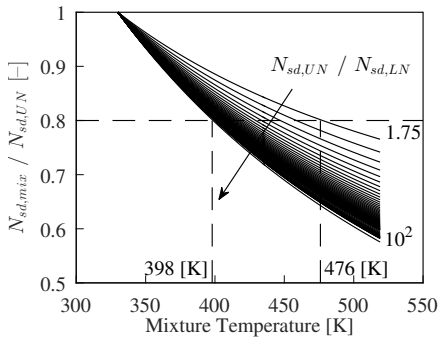

Figure 13: Resulting mixture seeding density due to UN and LN stream mixing as a function of blending quantity (i.e. mixture temperature) and seeding density ratio. The lower limit of 1.75 stems from the minimum required seeding density ratio, while the upper limit (100) is the approximate ratio of pixel saturation to background signal.

4.2.3. Strongly Reacting Fluid

The BTB configuration allows the stabilisation of low Da flames [26, 27] with chemical activity sustained by the external enthalpy source. By contrast, self–sustained flames at high Da detach from the stagnation plane [11, 29, 44] with both regimes present at intermediate Da. The chemically active state was accordingly segregated into fluids with low and high reactivity for $\Phi \geq 0.60$ as discussed in Sec. 3.4. The resulting thresholds are $\Lambda_{\mathrm{OH},q(0.6)} = 3.5$, $\Lambda_{\mathrm{OH},q(0.8)} = 5.5$ and $\Lambda_{\mathrm{OH},q(1.0)} = 5.8$ following Eq. (4). The threshold values $\Lambda_{\mathrm{OH},q}$ can be directly related to the limiting OH concentration determined in Sec. 3.4 and are summarised in Table 4.

$$\Lambda_{\mathrm{OH},q(\Phi)} = \frac{[\mathrm{OH}]_{q(\Phi)}}{[\mathrm{OH}]^{\ddagger}} \simeq \frac{I_{q(\Phi)}}{I^{\ddagger}} \tag{4}$$

The strongly reacting fluid probability is defined as $I \geq I_{q(\Phi)}$. An example of the OH intensity ratio PDF for a stoichiometric DME/air flames ($Da = 5.6$) is shown in Fig. 4. A large proportion of the samples exceed $\Lambda_{\mathrm{OH},q(1.0)}$ and a bimodal tendency, consistent with flamelet burning, is observed.

Table 4: Summary of the thresholds ($\Lambda_{\mathrm{OH},p}$ and $\Lambda_{\mathrm{OH},q(\Phi)}$) and approximate OH concentrations (in 10^{-2} mol/m^3) to delineate the fluid states as discussed in Sec. 4.

Φ	0.20	0.40	0.60	0.80	1.0
$\Lambda_{\mathrm{OH},p}$			2.0		
$[\mathrm{OH}]_p$			1.76		
$\Lambda_{\mathrm{OH},q(\Phi)}$	–	–	3.5	5.5	5.8
$[\mathrm{OH}]_q$	–	–	3.1	4.9	5.1

4.2.4. Weakly Reacting Fluid

The definition of fluid parcels with intermediate OH intensities between the extinction limit and the HCP follows directly from Eq. (5).

$$\Lambda_{\mathrm{OH},p} < \frac{I}{I^{\ddagger}} < \Lambda_{\mathrm{OH},q(\Phi)} \tag{5}$$

Intermediate OH intensities can stem from (i) thermally supported combustion at rates of strain beyond the extinction point [11, 26, 29, 44], (ii) decay towards equilibrium in combustion products and (iii) ignition events. It is possible to delineate the weakly reacting fluid state further via additional scalar information. However, in the current work the overall significance of the fluid state is explored as a function of Da. The methodology of Hampp and Lindstedt [44] is here simplified by using the same product fluid threshold ($\Lambda_{\mathrm{OH},p} = 2.0$) for all cases. The mildly reacting fluid [44] is accordingly renamed weakly reacting.

4.3. Spatial Multi-Fluid Resolution

The spatial (planar) resolution of the multi-fluid algorithm is limited by spatial filtering of the density segregation technique and was determined by means of an USAF-1951 test target [96]. The image of the test target was subjected to the spatial filtering algorithm and the smallest resolvable line pair was defined as the multi-fluid resolution, i.e. $\lambda_{MF} = 250$ µm [44]. Thin

Table 5: Physical and resolved length scales in µm, λ_{PIV} is the PIV and λ_{MF} the multi-fluid resolution. The minimum laminar flame thickness at $\Phi = 1.0$ is $\min(\delta_f)$, λ_D is the mean scalar dissipation layer thickness [97] and λ_B the Batchelor scale [98].

Scales	Reactants	HCP
λ_{PIV}	595	
λ_{MF}	250	
$\min(\delta_f)$	222	—
λ_D	621 ± 18	—
λ_B	86 ± 15	~ 370

layers below the multi-fluid resolution were reassigned to the adjacent fluid states via a 2D median filter. This applies to the sharply rising OH signal leading from reactants to the strongly reacting state. For the current flames such layers have a thickness below the multi-fluid resolution. An overview of relevant physical and resolved scales is provided in Table 5.

4.4. Velocity Conditioning

The benefits of analysing turbulent flames using conditional (bimodal) statistics are well established [33, 34, 85, 86, 99]. The multi–fluid classification permits conditioning on each fluid state, see Eq. (6), and thus the quantification of the evolution of velocity statistics as a function of Da. The instantaneous conditioning variable ($c_{FS,n}$) is defined as unity within the individual fluid state (FS) and nil elsewhere. Thus, only the velocity vectors within the bounding iso-contour of a fluid state are used.

$$
\begin{aligned}
\overline{U_{k,FS,i,j}} &= \frac{1}{N}\sum_{n=1}^{N} c_{FS,n,i,j}\cdot U_{k,n,i,j} \quad \forall\ i,j \\
(u'u')_{k,FS,i,j} &= \frac{1}{N}\sum_{n=1}^{N} c_{FS,n,i,j}\cdot \left(U_{k,n,i,j} - \overline{U_{k,FS,i,j}}\right)^2 \quad \forall\ i,j \\
C_{FS,i,j} &= \frac{1}{N}\sum_{n=1}^{N} c_{FS,n,i,j} \quad \forall\ i,j
\end{aligned}
\tag{6}
$$

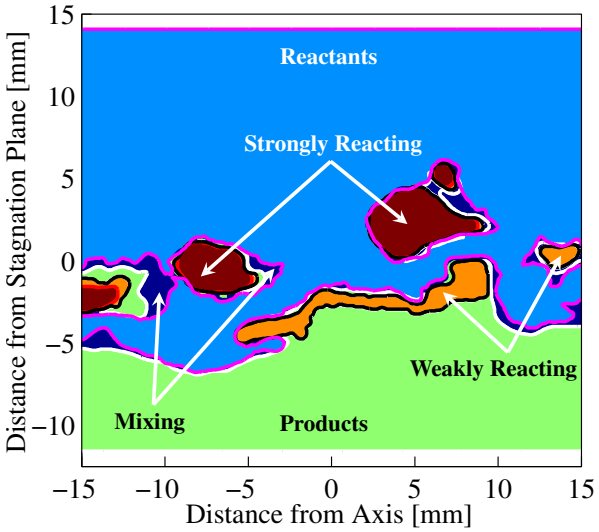

Figure 14: Example of a multi–fluid field for a DME / air flame at $\Phi = 0.80$: Light blue – **reactant fluid**, dark blue – **mixing fluid**, orange – **weakly reacting fluid**, red – **strongly reacting fluid** and green – **product fluid**. The pink iso–contour encloses the reactant fluid, the white iso–contour encloses all OH signal, the black iso–contour encloses the weakly reacting fluid, the red iso–contour encloses the strongly reacting (flamelet) fluid and the mixing fluid is bordered by the pink and white iso–contour.

In Eq. (6), k denotes a velocity component, n the instantaneous image, N the total number of images (3000) with i and j the index variables. The resulting fluid state progress variable (C_{FS}) is a reaction progress variable [8] with $\sum_{FS} C_{FS} = 1$.

5. Results and Discussion

The distribution of the different fluid states with a variation in the Damköhler number (Da) is evaluated first followed by an analysis of the impact on the turbulent flow field by means of conditional and unconditional velocity statistics. An example of a resulting quinary multi–fluid field, corresponding to the image pair in Fig. 10, is depicted in Fig. 14.

5.1. Multi–Fluid Statistics

Minor inconsistencies of the stagnation plane location may arise due to jet momentum matching. Hence, the spatial multi–fluid probabilities were evaluated along x_s as shown in Fig. 2. The origin ($x_s = 0$) is aligned with the first thermal alteration of the fluid, i.e. the density segregation iso–contour obtained from Mie scattering. Inherently, the reactant fluid probability drops sharply from unity to zero at the origin as shown in Fig. 15a. However, it re-emerges downstream, extending to one integral length scale of turbulence with its peak at $\sim L_I/4$. The effect is independent of Da and accordingly related to turbulent transport. The recurrence can be caused by large eddies tearing out pockets of unburnt reactants and/or a three-dimensional effects. Nevertheless, the probability remains ≤ 5 % for all cases.

The probability of finding mixing fluid is shown in Fig. 15b. A sharp rise to 90 % at the origin provides evidence of the importance of this fluid state – particularly for flows with $Da \leq 1$. At high reactivity, i.e. $\Phi \geq 0.80$, the peak probability of the mixing fluid in direct proximity of the origin is significantly reduced. This suggests an immediate onset of chemical activity adjacent to the reactant fluid, without the necessity of HCP support. Moreover, with gradually increasing mixture reactivity the mixing fluid probability is reduced away from the origin in favour of chemical reactions, i.e. smaller quantities of HCP are required to initialise chemical activity. The interface statistics presented by Hampp and Lindstedt [44] showed self-sustained flames directly adjacent to the reactants for $Da > 1$. By contrast, supported burning regions at $Da \leq 1$ were separated from the reactants by an interlayer acting as thermal support. The spatial extent of the mixing fluid is essentially limited by L_I suggesting a correlation with turbulent transport.

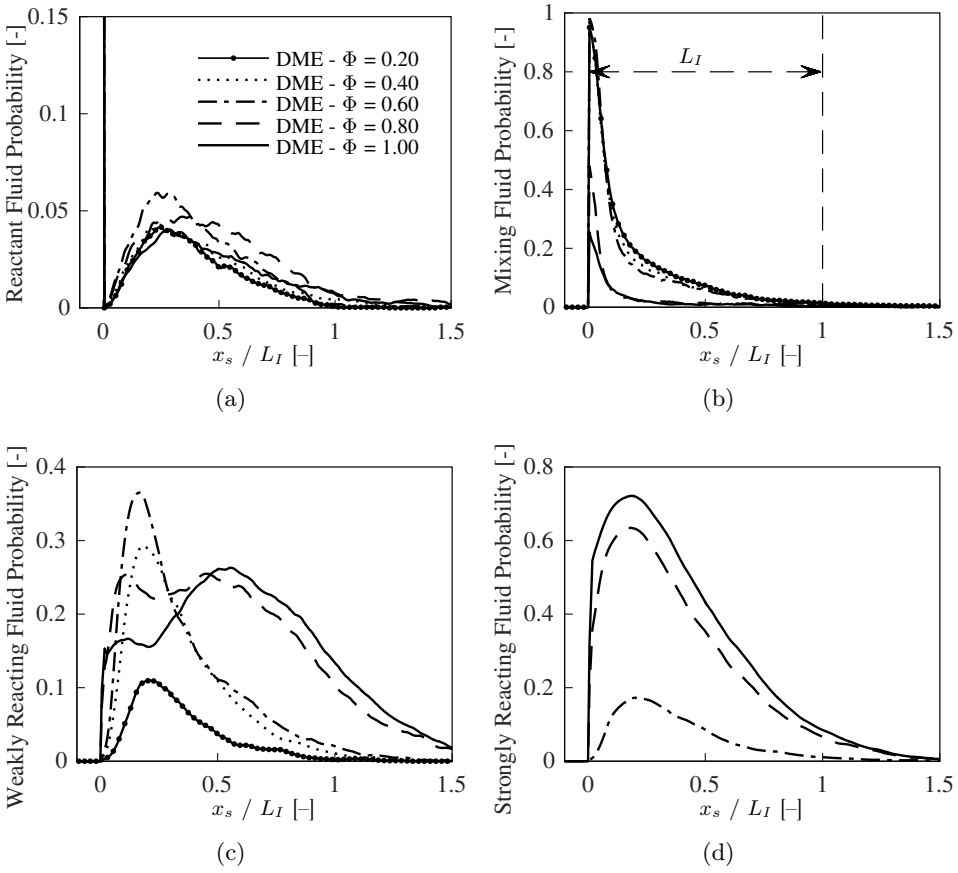

Figure 15: Multi–fluid probability for DME cases at $\Phi = 0.20 - 1.0$: (a) Reactant fluid; (b) Mixing fluid; (c) Weakly reacting fluid; (d) Strongly reacting (flamelet) fluid probability. The markers on the DME – $\Phi = 0.20$ line are drawn for identification purposes and do not represent the spatial resolution. The HCP fluid contributes the residual percentiles.

The probabilities of encountering regions with weakly and strongly reacting fluids were also determined. With a decreasing chemical timescale the weakly reacting fluid gains significance as shown in Fig. 15c with the magnitude and spatial extent enhanced. The reduction in the peak probability for mixtures with $Da > 1$ is a consequence of the augmentation of the strongly reacting (flamelet) fluid probability, see Fig. 15d, as self-sustained burning

is increasingly realised. The peak probability of the strongly reacting fluid reaches 63 % and 71 % for $\Phi = 0.80$ and 1.0 – approximately twice that of the corresponding weakly reacting fluid. For mixtures with $\Phi \geq 0.60$ the chemically active fluid states spatially extend beyond L_I due to dilatation.

Area based data highlights the impact of mixture reactivity on fluid pocket sizes. The normalised average areas ($\alpha = A_{FS,\Phi}/A_{r,\Phi}$) were determined for all Φ, as shown in Fig. 16, and illustrate the increasing importance of a multi–fluid analysis for flows with $Da < 1$:

- The mixing fluid island size increases with decreasing Da (around a factor of four compared to $\Phi \geq 0.80$) and exceeds the weakly and strongly reacting fluid sizes for flows with $Da < 1$.
- For the transitional case ($\Phi = 0.60$) the average size of mixing, weakly and strongly reacting pockets are similar.
- The average size of continuous weakly reacting fluid pockets reduces with decreasing Da giving values of 62 %, 20 %, 17 % and 10 % relative to the stoichiometric flame for $\Phi = 0.80$, 0.60, 0.40 and 0.20.
- The average size of strongly reacting fluid areas reduce by a factor of six with a change in the stoichiometry from $\Phi = 1.0$ to $\Phi = 0.60$.

5.1.1. Sensitivity Analysis

The impact of thresholds on statistics was explored using a sensitivity analysis for all cases featuring all fluid types ($\Phi \geq 0.60$). The estimated Da numbers suggest that for $\Phi = 0.60$ conditions are close to a transition from the thin reaction zone regime to distributed reactions and for $\Phi = 1.0$ from the corrugated flamelet regime to thin reaction zones.

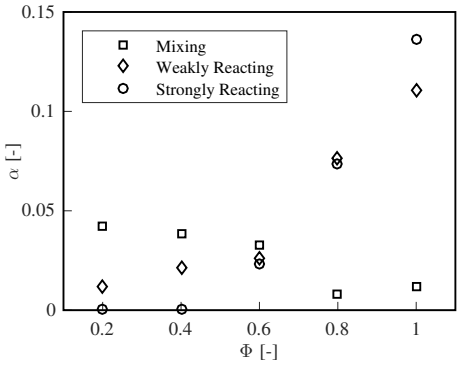

Figure 16: The average multi–fluid area size was determined for the intermediate fluid states (FS) and normalised by the reactant fluid area at respective Φ ($\alpha = A_{FS,\Phi}$ / $A_{r,\Phi}$).

The product fluid threshold $\Lambda_{\mathrm{OH},p}$ separating hot combustion products from the weakly reacting fluid was varied between 1.6 – 2.4. The range starts below the OH intensity ($\sim$ 1.8) associated with oxidation of the residuals in the HCP products. Results shown in Fig. 17a are aligned at $x_s = 0$ and highlight a reduction of the peak probability of the weakly reacting fluid, yet the spatial extent and general trend of the distributions are preserved.

The sensitivity of the strongly reacting (flamelet) burning mode probability was investigated by applying a threshold variation from below the twin flame extinction point with a symmetric shift around the defined thresholds, i.e. $3.0 < \Lambda_{\mathrm{OH},q(\Phi=0.6)} < 4.0$, $5.0 < \Lambda_{\mathrm{OH},q(\Phi=0.8)} < 6.0$ and $5.0 < \Lambda_{\mathrm{OH},q(\Phi=1.0)} < 6.5$. The variations are much larger than the differences between the twin flame and BTB burning modes (see Sec. 3.4) and similar to the change in the twin flame OH concentration from nearly unstrained conditions ($a = 75\ \mathrm{s}^{-1}$) to the extinction point (a_q) for the respective Φ. The results are shown in Fig. 17b. A reduction in the peak probability is noted, while the spatial extent and distribution trend remains. It is apparent that even with the large variations applied, the probability of finding weakly reacting fluid

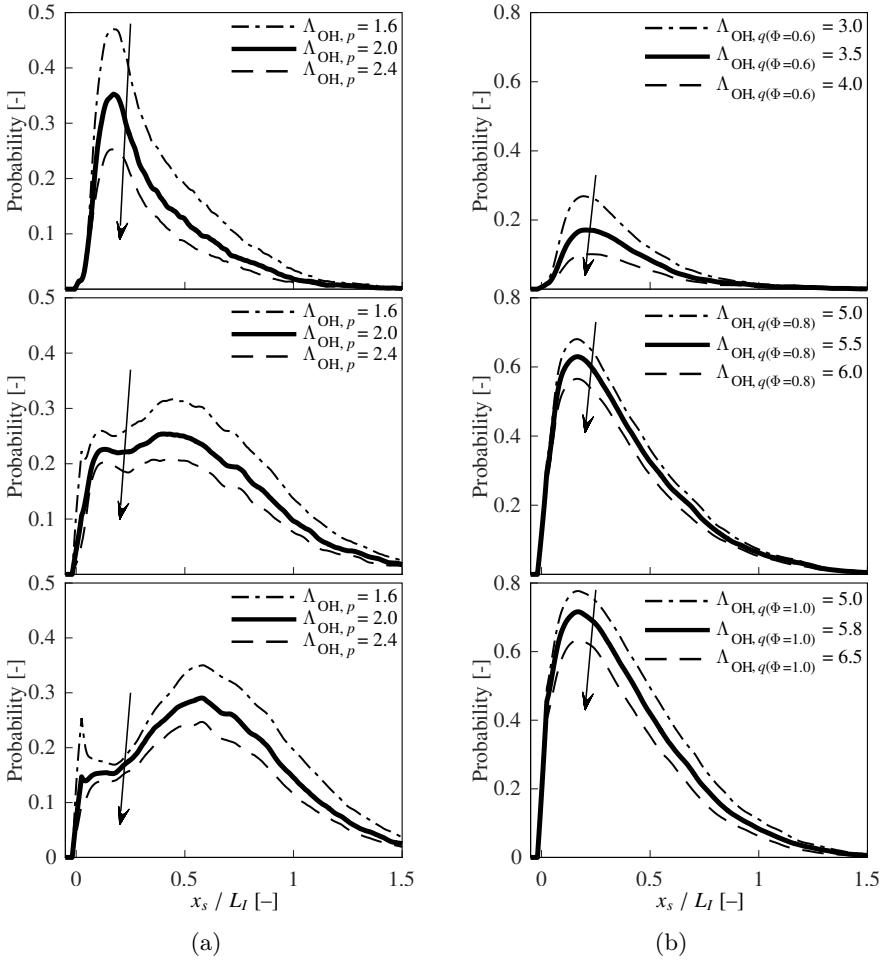

Figure 17: Sensitivity analysis on threshold definitions: (a) Impact on weakly reacting fluid probabilities of the product fluid threshold ($\Lambda_{\mathrm{OH},p}$) for $\Phi = 0.60$ (top row), $\Phi = 0.80$ (middle row) and $\Phi = 1.0$ (bottom row); (b) Impact on the strongly reacting fluid probabilities of the delineating threshold ($\Lambda_{\mathrm{OH},q(\Phi)}$) for $\Phi = 0.60$ (top row), $\Phi = 0.80$ (middle row) and $\Phi = 1.0$ (bottom row); Arrows indicate increasing threshold values.

is 36 $\pm$ 11 % for the transitional case with $Da \simeq 1$ ($\Phi = 0.60$). The corresponding probability of finding strongly reacting (e.g. flamelet) fluid is 18 $\pm$ 8 %. At higher Da ($\Phi \geq 0.80$), the weakly reacting fluid peak probability is around 28 %, while the strongly reacting fluid peak probability is

augmented to 71 ± 7 % for the stoichiometric case.

To further assess the uncertainty of the multi-fluid analysis, the rms of the spatial displacement ($\Delta_{x,FS}$) was evaluated for the leading edge of all iso-contours via Eq. (7), where θ is the individual and Θ_{FS} the total number of thresholds for a fluid state (FS).

$$\bar{x}_{FS} = \frac{\sum_{\theta=1}^{\Theta_{FS}} x_{FS,\theta}}{\Theta_{FS}} \; ; \qquad \Delta_{x,FS} = \left(\frac{\sum_{\theta=1}^{\Theta_{FS}} (\bar{x}_{FS} - x_{FS,\theta})^2}{\Theta_{FS}} \right)^{0.5} \tag{7}$$

The spatial locations of the reactant and mixing fluid iso-contours are nearly independent of the threshold value with a $\Delta_{x,FS} < 25$ µm. The weakly reacting and product fluid iso-contours exhibit uncertainties of 350 µm and 308 µm (similar to the multi-fluid resolution) due to the relatively smooth OH gradients. An uncertainty of ~ 70 µm (similar to the Kolmogorov length scale) was determined for the strongly reacting fluid iso-contour.

5.2. Multi-Fluid Flow Structure

The analysis presented by Hampp and Lindstedt [44] is here extended to include the flow direction across fluid interfaces encountered by traversing along the theoretical stagnation point streamline from reactants to products. The sign of the unit vector of the streamline tangent $\hat{\mathbf{s}}$ is defined as positive in the flow direction and the unit vector of the iso-contour normal $\hat{\mathbf{n}}$ is positive from reactants to products. Three flow scenarios were used: (i) The tangent of the streamline is approximately aligned with the iso-contour normal so that $\hat{\mathbf{s}} \cdot \hat{\mathbf{n}} > 0.05$, (ii) the opposite case with $\hat{\mathbf{s}} \cdot \hat{\mathbf{n}} < -0.05$ and (iii) tangential flow with $||\hat{\mathbf{s}} \cdot \hat{\mathbf{n}}|| < 0.05$ (i.e. 72° – 108°). A schematic is provided in Fig. 18a. The diagrams in Figs. 18b-18d show the major flow

paths (≥ 5 %) for $\Phi = 0.20$, 0.60 and 1.0 with the flow direction indicated by the arrows. The stoichiometric case (Fig. 18b) exhibits a flamelet-like structure with a preferential flux from reactants into the strongly reacting fluid. However, high rates of strain [44] cause secondary fluxes into the mixing and weakly reacting fluid. By contrast, the primary flux for $\Phi = 0.20$, see Fig. 18d, passes through the mixing fluid. The substantial negative or close to perpendicular orientation of $\hat{\mathbf{s}}$ to $\hat{\mathbf{n}}$ at the mixing fluid interfaces illustrate a reaction onset that is governed by the HCP interactions. The reaction onset for the transitional case ($Da \simeq 1$, see Fig. 18c) is also governed by the thermal support and the mixing – weakly reacting interface does not show a preferential flux direction due to high vorticity levels in the proximity of the stagnation plane [44].

The OH gradients were also calculated along the theoretical stagnation point streamline using Eq. (8), where $I_n/I^{\ddagger}$ is the normalised instantaneous OH signal intensity with a resolution $\delta_x = 37.2$ µm.

$$\nabla I_n = \frac{(I_n/I^{\ddagger})_{i+1} - (I_n/I^{\ddagger})_{i-1}}{2\delta_x} \tag{8}$$

High frequency fluctuations of the instantaneous gradient (∇I_n) were removed by means of a moving average filter (length $\approx \lambda_{MF}$). The mean resolution of the instantaneous 5 – 95 % OH profile was 22±12 pixels. Laminar BTB counterflow calculations (see Sec. 3.4) provide theoretical limits for flamelet-like structures. Characteristic OH gradients can also readily be extracted. The weakly strained self-sustained flames ($a = 0.1 \cdot a_b = 75$ s^{-1}) are used to define the first limit and the maximum rate of strain (see Table 3) encountered in the current configuration ($a \simeq 4000$ s$^{-1} > a_q$) provides the second limit. At high rates of strain, the OH gradients reduce as a result

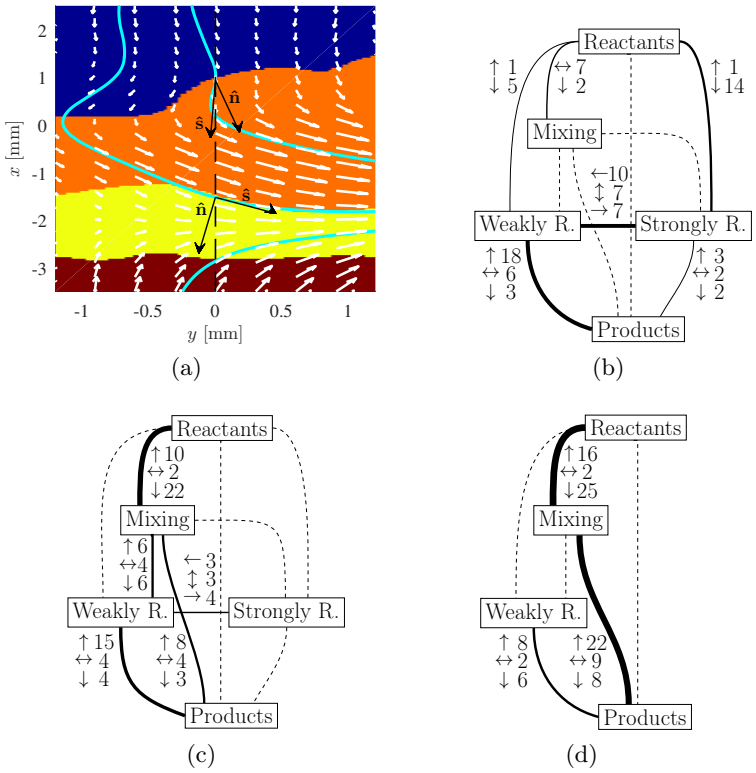

Figure 18: (a) Sample multi-fluid image for DME / air at $\Phi = 0.80$ with streamlines (cyan curves) and PIV vectors overlaid: Blue – Reactants, Orange – Strongly Reacting, Yellow – Weakly Reacting, Red – Products. The black vertical dashed line shows the theoretical stagnation point streamline and the arrows the unit vectors of the iso-contour normal ($\hat{\mathbf{n}}$) and streamline tangent ($\hat{\mathbf{s}}$). The diagrams show the multi-fluid flow structure for (b) $\Phi = 1.0$, (c) $\Phi = 0.60$ and (d) $\Phi = 0.20$. The weighted connections and values illustrate the number of interfaces in % and the arrows indicate the flow direction ($\updownarrow$ with $\leftrightarrow$ indicating near tangential flow). The total numbers of interfaces are 12000, 9700 and 7600 for $\Phi = 1.0$, 0.60 and 0.20.

of the HCP support and the second limit accordingly presents an approximate minimum. However, lower values are possible and can be attributed to turbulent mixing or distributed ignition events. The weakly strained flames provide the approximate upper gradient limit. The normalised PDFs of the maximum ∇I_n are depicted in Fig. 19 for $\Phi = 0.20$, 0.60 and 1.0. The PDF of the stoichiometric case shows a strong flamelet-like behaviour with

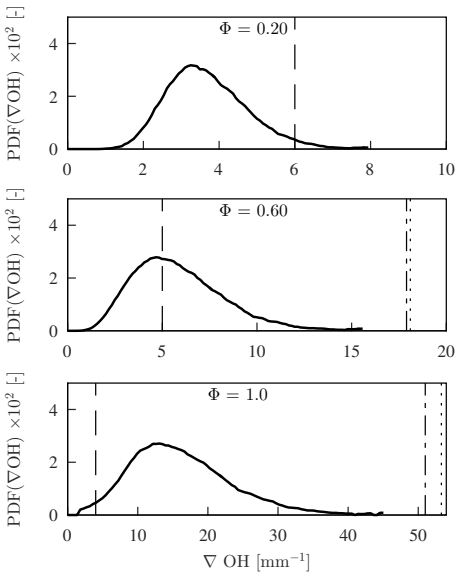

Figure 19: Normalised PDF of the maximum OH gradient for $\Phi = 0.20$ (top) 0.60 (middle) and 1.0 (bottom row). The vertical lines show the maximum gradient for the weakly strained ($a = 75$ s^{-1}, - · - · -) and HCP dominated ($a = 4000$ s^{-1}, - - -) flames determined from laminar BTB counterflow calculations. The maximum OH gradients in the corresponding twin flames over the range $75 < a$ [s^{-1}] $< a_q$ are also shown (·····).

gradients bounded by the determined limits. With decreasing Φ, the PDF shifts to reduced gradients as the OH producing reactions are increasingly governed by HCP support. The PDF for $\Phi = 0.20$ shows gradients consistently below the lower flame limit. The transitional case with $\Phi = 0.60$ ($a_q = 600$ s$^{-1} < a_b$) also shows a significant impact of the HCP support, which is consistent with the above vector based analysis and the study by Hampp and Lindstedt [44].

5.3. Velocity Field along the Burner Axis

The normalised mean axial ($\overline{U}/U_b$) velocity component along the stagnation point streamline is shown in Fig. 20. The locations of the burner nozzles are at $x/D = 0.50$ (UN providing DME/air reactants) and $x/D =$

-0.50 (LN providing HCP). To enhance the readability, the panels in Fig. 20 are separated showing cases with $Da < 1$ in the left column and $Da \geq 1$ in the right column. In the proximity of the UN exit ($x/D > 0.2$) the $\overline{U}/U_b$ ratio is not affected by the mixture reactivity as shown in the top row of Fig. 20. The impact of combustion on $\overline{U}/U_b$ becomes evident at $x/D \leq 0.2$ by an eased and lagged deceleration of the mean flow with increasing Φ. This is caused by an earlier onset of combustion and more pronounced flow acceleration towards the HCP (x/D = -0.50) with increased heat release.

The axial and radial fluctuations ($\sqrt{u'u'}/U_b$ and $\sqrt{v'v'}/U_b$) are depicted in the middle and bottom rows of Fig. 20 with the same subdivision. At $x/D > 0.2$ both components are independent of the mixture reactivity. For $x/D < 0.2$ the velocity fluctuations are reduced with increasing mixture reactivity. A double peak of $\sqrt{u'u'}/U_b$ gradually emerges at $\Phi \geq 0.60$, see middle row right column of Fig. 20, which is not observed at lower reactivities. The location of the peak closer to the UN ($x/D = 0.50$) corresponds to an iso-contour $\overline{c} = 0.05$ and is shifted towards the reactants with increasing Da due to the higher burning velocities. The shift for the stoichiometric case relative to that with $\Phi = 0.80$ is 1.8 mm ($\sim L_I/2$). The second peak indicates the location of the mean interaction of the opposing streams. The strong dilatation effects and associated flow acceleration, pushes the stagnation plane towards the HCP as evident in Fig. 20 (top and middle row of right column). Similar trends were observed by Goh et al. [11, 12] at lower turbulence levels. The combustion mode transition is sufficiently strong to significantly impact the flow field.

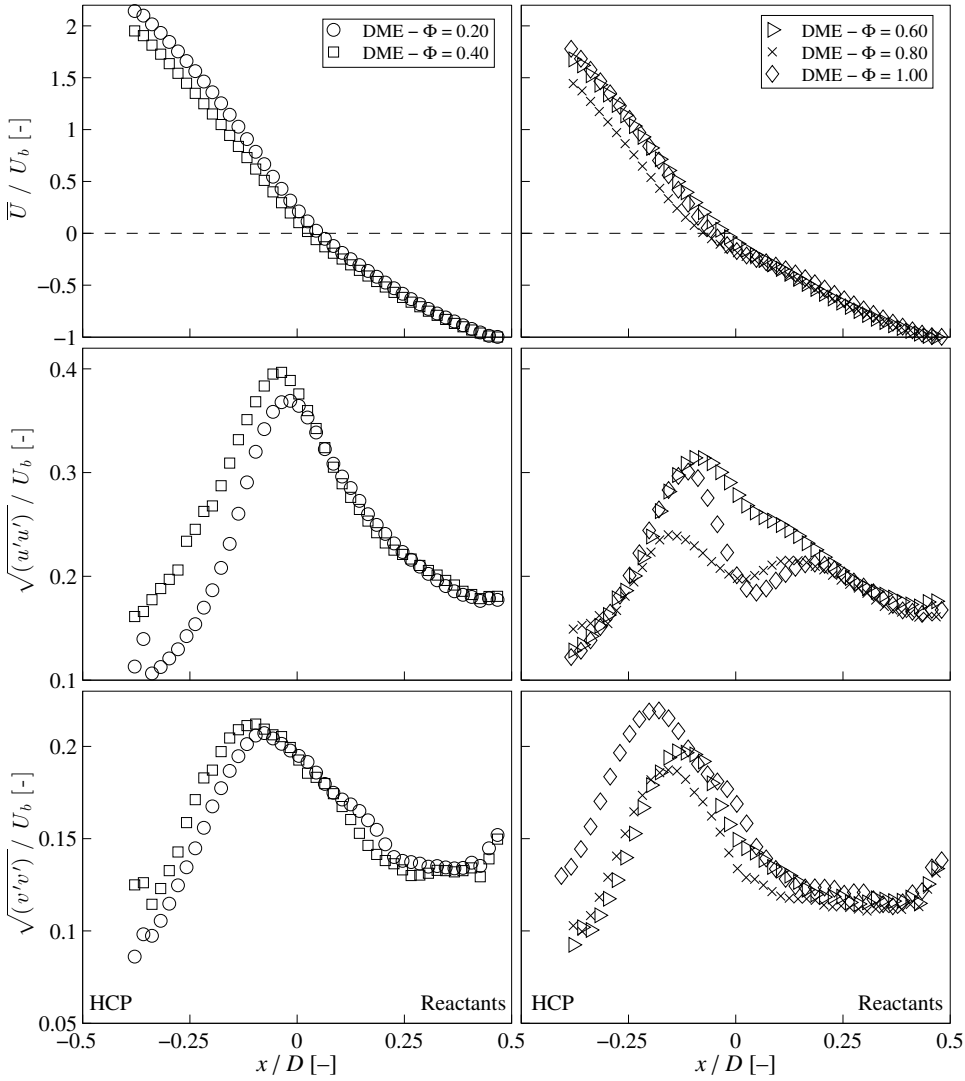

Figure 20: Unconditional velocity and its fluctuation along the centre axis: Mean axial velocity (top), axial (middle) and radial velocity fluctuation (bottom) for $Da < 1$ (left) and $Da \geq 1$ (right). The HCP boundary is located at x/D = -0.50 and the DME/air reactants at $x/D = 0.50$. Only every second data point is drawn to enhance the readability.

5.4. Conditional Velocities along the Burner Axis

The conditional velocities, see Sec. 4.4, are here discussed along the theoretical stagnation point streamline and aligned at the origin $x_s = 0$. A minimum of 75 vectors was used and the error bars indicate the impact of the variation of the thresholds, as used in the sensitivity analysis in Sec. 5.1.1, on the conditional velocity statistics.

5.4.1. Conditional Reactant Fluid Velocity

The conditional mean axial reactant velocity ($\overline{U_{0,r}}/U_b$) and turbulent fluctuations ($\sqrt{(u'u')_{0,r}}/U_b$ and $\sqrt{(v'v')_{0,r}}/U_b$) are shown in Fig. 21. The stronger compression of the mean axial flow with increasing Da, observed for the unconditional axial velocity (see Fig. 20), remains as shown in the top row. At the origin, $\overline{U_{0,r}}/U_b$ increases with Φ, indicating an earlier reaction onset and a detachment from the stagnation plane. The conditional reactant velocity fluctuations are shown in the middle and bottom rows. The increasing separation of the axial and radial velocity fluctuations with Φ at $x_s < 0$ is caused by the shift of the first thermal alteration towards the reactants. The occurrence of reactant fluid pockets beyond the origin stems from turbulent transport. While the probability (Fig. 15a) is independent of the Damköhler number the resulting flow condition varies with Φ. With increasing reactivity, the pockets exhibit significantly reduced fluctuations and a larger (more negative) axial velocity (see Fig. 21 top row), i.e. are accelerated away from the location of the reaction onset with the motion of the pocket increasingly driven by dilatation (e.g. strongly reacting fluid) [44]. The threshold definition has a vanishing impact on the conditional reactant fluid velocity and its fluctuations.

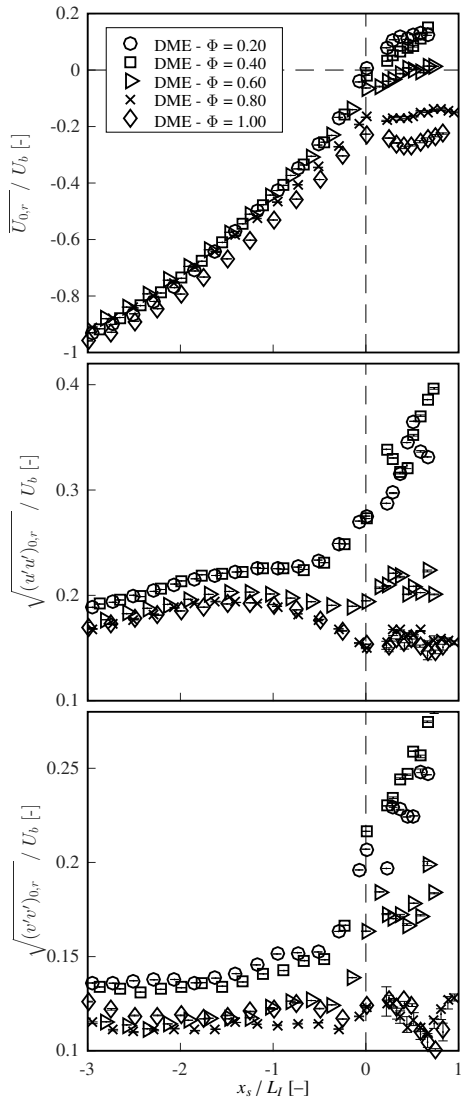

Figure 21: Conditional mean axial reactant velocity and its fluctuation aligned at the Mie scattering iso–contour: Top – $\overline{U_{0,r}}/U_b$; Middle – $\sqrt{(u'u')_{0,r}}/U_b$; Bottom – $\sqrt{(v'v')_{0,r}}/U_b$. Reactants at $x_s/L_I \leq 0$ and fluid pockets of reactants at $x_s/L_I > 0$. At $x_s/L_I < 0$ only every third data point is plotted to enhance the readability. At $x_s/L_I > 0$ all data points are shown. The bars show the uncertainty introduced by the threshold variation.

5.4.2. Conditional Mixing Fluid Velocity

The conditional mean axial mixing fluid velocity $\overline{U_{0,mix}}/U_b$ and axial and radial ($\sqrt{(u'u')_{0,mix}}/U_b$, $\sqrt{(v'v')_{0,mix}}/U_b$) turbulent fluctuations are depicted in Fig. 22. Away from the origin (i.e. $x_s/L_I > 0.25$) and for $\Phi \geq 0.80$ the mixing fluid velocity suffers from an insufficient number of realisations (see Fig. 15b) and is accordingly excluded.

For HCP supported combustion ($Da \leq 1$) the conditional mixing fluid velocities essentially coincide (top row) in the proximity of the origin. Differences towards progressively reduced velocities with increasing reactivity emerge at $x_s/L_I > 0.25$. The mixing velocities are significantly higher than the reactant velocities (compare Fig. 21), which suggests HCP addition leading to increased momentum in the direction towards the reactants. For flows with $Da > 1$, a distinct drop in $\overline{U_{0,mix}}/U_b$ and in turbulence velocities ($\sqrt{(u'u')_{0,mix}}/U_b$ and $\sqrt{(v'v')_{0,mix}}/U_b$) is evident. At low Da, the reactants accommodate more heat addition. Hence, increased amounts of combustion products that alter or govern the mixing fluid flow dynamics lead to a gradual alignment of $\overline{U_{0,mix}}/U_b$ with the HCP flow direction. This highlights the increasing need for thermal support to initialise the oxidation process for flows with $Da \leq 1$ and suggests a gradual combustion regime transition away from self–sustained burning towards a supported mode. Once more, the threshold definition has a negligible impact on the conditional mixing fluid velocity and its fluctuations.

5.4.3. Conditional Weakly Reacting Fluid Velocity

Results obtained using velocity conditioning on the weakly reacting fluid are shown in Fig. 23. Similarly to the mixing fluid, the conditional mean axial velocity (top row) reveals an increasingly HCP driven flow with de-

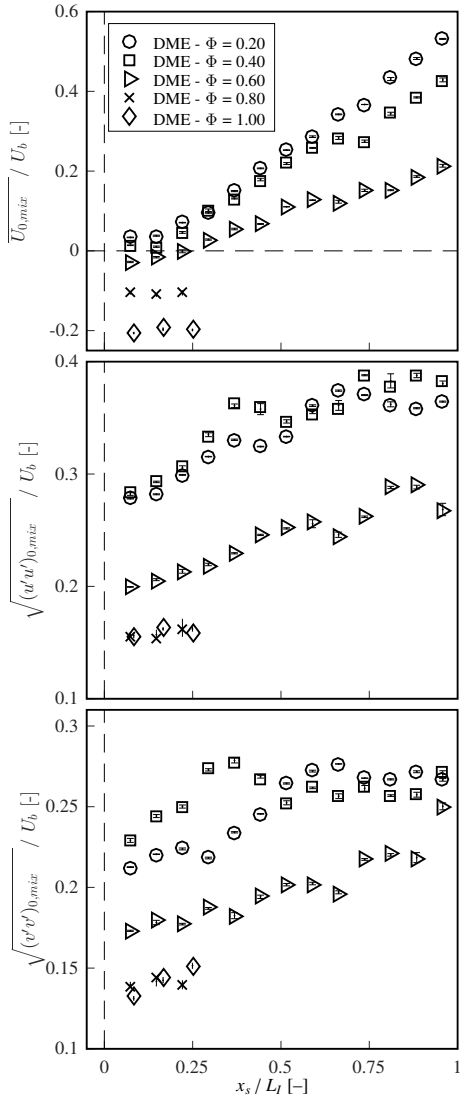

Figure 22: Conditional mean axial mixing velocity and its fluctuation aligned at the Mie scattering iso–contour: Top – $\overline{U_{0,mix}}/U_b$; Middle – $\sqrt{(u'u')_{0,mix}}/U_b$; Bottom – $\sqrt{(v'v')_{0,mix}}/U_b$. Reactants are at $x_s/L_I \leq 0$ and mixing fluid at $x_s/L_I > 0$. The bars show the uncertainty introduced by the threshold variation.

creasing Da. Mixtures with $\Phi \geq 0.80$ lead to negative $\overline{U_{0,weak}}/U_b$ in the direct proximity of the origin (i.e. in line with the natural UN reactant flow direction). For leaner mixtures, $\overline{U_{0,weak}}/U_b$ becomes positive and directed towards the reactants. The more moderate slope of $\overline{U_{0,weak}}/U_b$ and distinctly reduced axial velocity fluctuations ($\sqrt{(u'u')_{0,weak}}/U_b$, see middle row of Fig. 23) with increasing Φ can be attributed to the enhanced dilatation. The radial fluctuations (bottom row) show significant scatter with a trend suggesting a reduction with increasing Da in the direct proximity of the origin yet consistently approach $\sqrt{(v'v')_{0,weak}}/U_b \approx 0.25$ at $x_s \gg 0$. The observations highlight the reduced influence of HCP addition with increasing mixture reactivity. The threshold definition has a modest impact on the conditional weakly reacting fluid velocity statistics.

5.4.4. Conditional Strongly Reacting (Flamelet) Fluid Velocity

The conditional strongly reacting fluid velocity and turbulent fluctuations, see top row of Fig. 24, were evaluated for $Da \geq 1$ (i.e. $\Phi = 0.60$, 0.80, 1.0). The self-sustained flames are detached from the stagnation plane and are anchored in low compressive strain regions around or below the twin flame extinction point [44]. The conditional axial weakly and strongly reacting flow velocities are of the same magnitude in the direct proximity of the origin (compare top rows of Figs. 23 and 24). Away from the origin $\overline{U_{0,weak}}/U_b$ is governed by HCP addition, while $\overline{U_{0,str}}/U_b$ is driven by dilatation. This results in an axial flow acceleration towards the stagnation plane leading to a distinctly more negative $\overline{U_{0,str}}/U_b$ at $x_s > 0$. The value of $\overline{U_{0,str}}/U_b \rightarrow 0$ at $x_s/L_I \geq 0.75$ for $\Phi = 0.80$, while the stoichiometric case is aligned with the reactant flow direction (i.e. negative velocities). The conditional axial fluctuations of the strongly reacting fluid, see middle row

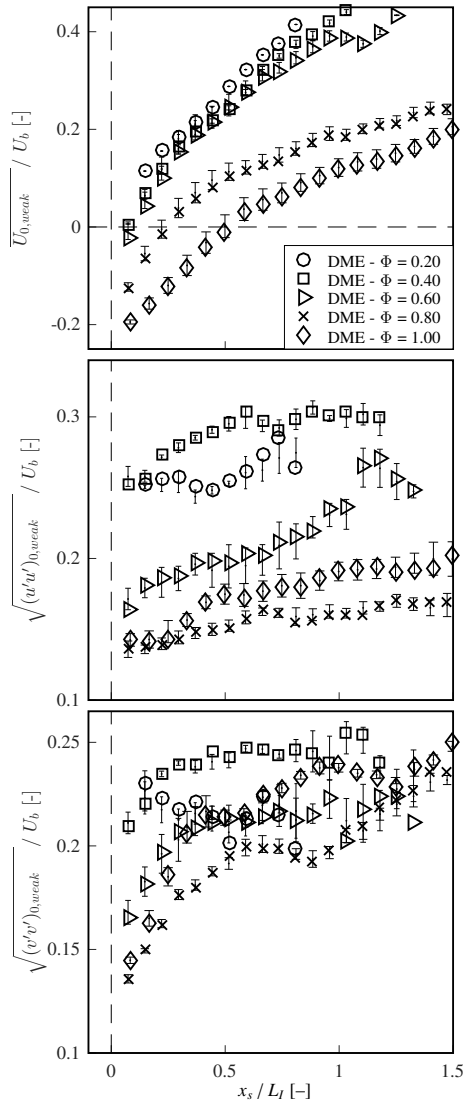

Figure 23: Conditional mean axial weakly reacting velocity and its fluctuation aligned at the Mie scattering iso–contour: Top – $\overline{U_{0,weak}}/U_b$; Middle – $\sqrt{(u'u')_{0,weak}}/U_b$; Bottom – $\sqrt{(v'v')_{0,weak}}/U_b$. Reactants are at $x_s/L_I \leq 0$ and weakly reacting fluid at $x_s/L_I > 0$. The bars show the uncertainty introduced by the threshold variation.

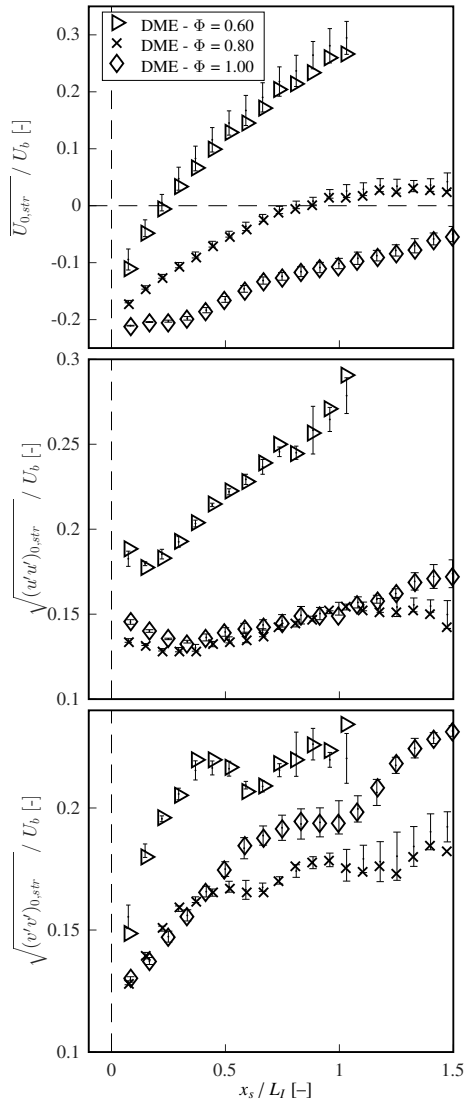

Figure 24: Conditional mean axial strongly reacting velocity and its fluctuation aligned at the Mie scattering iso–contour: Top – $\overline{U_{0,str}}/U_b$; Middle – $\sqrt{(u'u')_{0,str}}/U_b$; Bottom – $\sqrt{(v'v')_{0,str}}/U_b$. Reactants are at $x_s/L_I \leq 0$ and strongly reacting fluid at $x_s/L_I > 0$. The bars show the uncertainty introduced by the threshold variation.

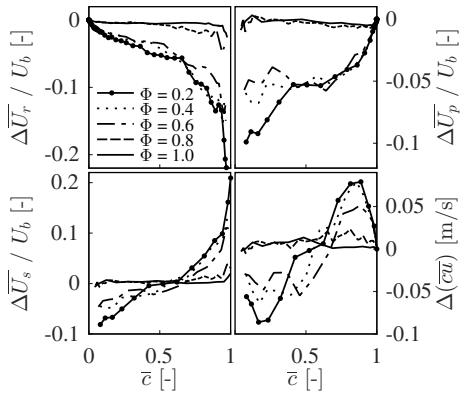

Figure 25: Limitation of a bimodal description evaluated by the difference (Δ) between a particle density and OH signal based segregation technique along the reaction progress $\overline{c}$. Discrepancy of the mean axial reactant fluid (top left), product fluid (top right) and slip (bottom left) velocity as well as scalar flux (bottom right).

of Fig. 24, are distinctly reduced for $Da > 1$. The conditional strongly reacting fluid velocity statistics are somewhat affected by the threshold variation. However, a clear separation with Da remain.

5.5. Limitations of Bimodal Descriptions

Hampp and Lindstedt [44] used a PIV particle seeding density based bimodal segregation [34, 85, 86] to determine conditional reactant, product and slip velocities as well as scalar fluxes. An alternative segregation technique is based on the OH–PLIF [100, 101] signal. Differences (Δ) in results between the two techniques provide an indication of the limitations of bimodal statistics as shown in Fig. 25. In the regime of self-sustained burning ($Da > 1$ and $\Phi \geq 0.80$) good agreement ($\Delta \simeq 0$) is obtained as at most a thin interface spatially separates the reactants from OH rich combustion products [44]. By contrast, at $Da \leq 1$ (i.e. $\Phi \leq 0.60$) substantial discrepancies emerge as the density segregation iso-contour detaches from OH containing fluids due to the mixing fluid interlayer.

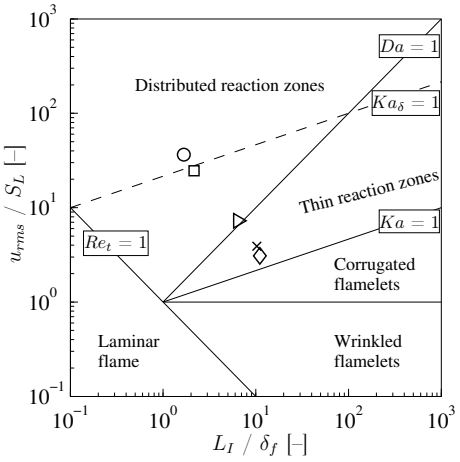

Figure 26: Flame conditions in a Borghi diagram [4]. Symbols as in Figs. 20 – 24.

5.6. Combustion Regime Classification

The estimated combustion modes based on Da are shown in Fig. 26. The corresponding (fine scale) Karlovitz number (Ka) requires the Kolmogorov length and time scales:

$$L_\eta = \left(\frac{\nu_r^3}{\varepsilon_r}\right)^{1/4} \qquad \tau_\eta = \sqrt{\frac{\nu_r}{\varepsilon_r}} \qquad Ka = \frac{\tau_c}{\tau_\eta} \tag{9}$$

The rate of dissipation (ε_r) in the reactants was estimated using the method of George and Hussein [102] for locally axi–symmetric turbulence Eq. (10).

$$\varepsilon_r = \nu_r \cdot \left[-\overline{\left(\frac{\partial u}{\partial x}\right)^2} + 2 \cdot \overline{\left(\frac{\partial u}{\partial y}\right)^2} + 2 \cdot \overline{\left(\frac{\partial v}{\partial x}\right)^2} + 8 \cdot \overline{\left(\frac{\partial v}{\partial y}\right)^2} \right] \tag{10}$$

Dissipation rates, Kolmogorov length and timescales and Ka are listed in Table 3. The dissipation rate was also used to estimate the total rate of

strain rate via the relationship of Kostiuk et al. [103]:

$$a_T = a_b + a_I = 2 \cdot \frac{U_b}{H} + \left(\frac{\varepsilon_r}{\nu_r}\right)^{1/2} \tag{11}$$

The bulk strain rate $a_b \approx 750\ \mathrm{s}^{-1}$ and the mean turbulent strain rate $a_I \approx 3200\ \mathrm{s}^{-1}$ lead to a total rate of strain of $a_T \approx 3950\ \mathrm{s}^{-1}$ ($> a_q$ for $\forall\ \Phi$) within the reactants (see Table 3). This suggests that thermal HCP support, required to sustain combustion beyond the conventional (strained twin flame) extinction limit, is likely to have some influence for all mixtures with conventional burning located in low strain regions – consistent with the above analysis.

The blending of HCP with the reactant fluid can cause auto–ignition. Accordingly, ignition delay times were computed for relevant initial temperatures (1000 – 1700 K) and equivalence ratios (Φ = 0.20 – 1.0) as shown in Fig. 6. The resulting auto–ignition based Da_{ign} is here related to turbulent mixing as shown in Eq. (12).

$$Da_{ign} = \frac{\tau_I}{\tau_{ign}} \tag{12}$$

The exponential temperature dependency of τ_{ign} suggests that ignition will occur close to the peak temperature within a fluid pocket. The expected range is bounded by the HCP temperature of 1700 K ($Da_{ign} = 214$; $\tau_{ign} =$ 12.6 µs) and the temperature ($\approx$ 1196 K; $\tau_{ign} = 2.5$ ms) giving $Da_{ign} = 1.0$. A corresponding auto–ignition Karlovitz number can readily be defined.

$$Ka_{ign} = \frac{\tau_{ign}}{\tau_\eta} \tag{13}$$

The auto–ignition process also depends on the bulk flow motion and

a third Damköhler number (Da_b), see Eq. (14), was defined based on a convection residence time τ_b ($\simeq$ 8.7 ms).

$$Da_b = \frac{\tau_b}{\tau_{ign}} \tag{14}$$

The τ_b was estimated by following the trajectory of a fluid parcel from the onset of reaction/mixing using a reaction progress variable iso–contour of $\bar{c}$ = 0.02 [33, 104] until it is convected out of the domain (i.e. $y = \pm 0.015$ m).

The computed Da_{ign} and Da_b and the corresponding Karlovitz number (Ka_{ign}) were used to derive the revised regime diagram shown in Fig. 27. On the right hand side of the Da_b line, unreacted mixture is likely to be convected out of the domain without ignition (assuming the absence of flame propagation). Left of the $1/Ka_{ign}$ line, the mixture is auto-igniting on a timescale shorter than the Kolmogorov timescale. The Da_b and $1/Ka_{ign}$ consequently bound the auto–ignition manifold for present study. The initial temperature (T_0) axis of this diagram can be considered a third dimension of a revised combustion regime diagram (see Figs. 26 and 27) which intersects at a given Re_t and T_0. The conventional Da numbers can readily be added to Fig. 27 at T_0 = 320 K. Under the current conditions (e.g. $Da_b > 700$ and $Ka_{ign} \approx 0.05$) any residual reactants will auto–ignite in the HCP. It is estimated that DME combustion in an auto–ignition mode can be sustained down to temperatures around 1200 K at the current Re_t. The overall analysis lends some support to conventional combustion regime diagrams. The high Damköhler number flame ($Da = 5.6$) is located close-to the corrugated flamelet regime and the current analysis shows a topological flamelet-like structure. By contrast, low Da combustion is dominated by thermal support and OH rich zones are spatially separated from the reactants.

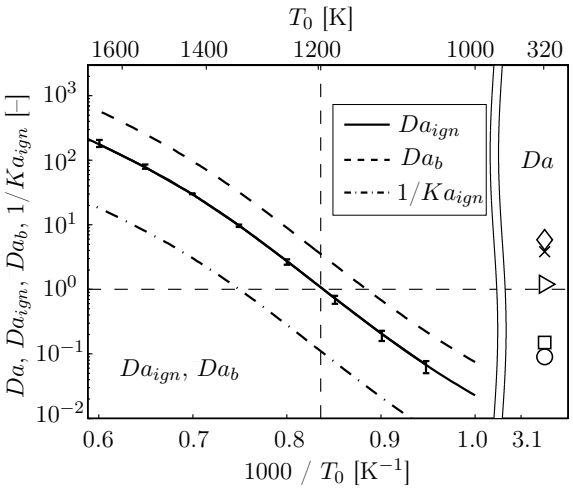

Figure 27: Auto–ignition Damköhler number based on the turbulent integral timescale (Da_{ign}), the bulk flow timescale (Da_b) and the inverse of the auto–ignition Karlovitz number ($1/Ka_{ign}$) as a function of initial temperature (T_0). The conventional Da for the different equivalence ratios (symbols as in Figs. 20 – 24) are also shown at $T_0 = 320$ K. The bars on the Da_{ign} line indicate the mixture impact ($\Phi = 0.20 - 1.0$).

6. Conclusions

The current study has investigated the probability of encountering selected fluid states as a function of the standard Damköhler number (Da). Based on a conventional combustion regime diagram, the conditions covered a transition from the corrugated flamelet regime to distributed reaction zones with $0.08 \leq Da \leq 5.6$. An opposed jet back–to–burnt configuration with fractal grid generated turbulence was used with a constant burnt gas state and the chemical time scale varied through the mixture stoichiometry. The mean turbulent strain (≥ 3200 s^{-1}) exceeded the extinction strain rate of the corresponding laminar flames for all mixtures.

The fluid states were analysed using a multi–fluid concept by means of simultaneous Mie scattering, OH–PLIF and PIV. Computations of strained

laminar flames in the directly corresponding geometry showed that the thermochemical state at the twin flame extinction point correlates well with flames in the back–to–burnt geometry at the same rate of heat release. For mixtures where the bulk strain ($\simeq 750$ s^{-1}) was similar to (or less than) the extinction strain rate, fluids with low and high reactivity could accordingly be segregated by a threshold based on the OH concentration at the extinction point leading to the identification of five fluid states: reactants, combustion products, mixing, weakly and strongly reacting (flamelet) fluids. A sensitivity analysis on the distribution between the fluid states was performed and it was shown that the observations are robust. The Damköhler number also has a significant impact on the spatial extent of the fluid states with large chemically active zones at high values and large mixing zones at low values. Moreover, high Damköhler number flames show a topological flamelet-like structure with steep OH gradients, while flames with Damköhler number ≤ 1 rely on thermal support that yields reduced OH gradients.

Velocity statistics show a distinct fluid acceleration due to increased heat release at high Damköhler number and that the flow field is dominated by hot combustion product addition for less reactive mixtures. Conditional velocity statistics were used to explain the impact on the evolution of different fluid states as a function of Da with the impact of interlayers separating reactants and products analysed in terms of limitations of bimodal descriptions.

Finally, the results were analysed in the context of auto–ignition based Da and Ka numbers and the conditions for a transition to a combustion mode dominated by the hot combustion product temperature estimated. Further delineation beyond the current five fluid states to quantify the probability of different types of reacting fluids (e.g. associated with low temperature ignition events) is possible through measurements of additional scalars.

7. Acknowledgements

The authors would like to acknowledge the support of the AFOSR and EOARD under Grant FA8655-13-1-3024 and thank Dr Chiping Li and Dr Russ Cummings for encouraging the work. The US Government is authorised to reproduce and distribute reprints for Governmental purpose notwithstanding any copyright notation thereon. The authors would also like to thank Dr Robert Barlow for his support, Prof Fokion Egolfopoulos and Dr Yang Wang for supplying strained flame extinction data and Mr. Bernhard Wieneke for the discussion on adaptive PIV.

8. References

[1] I. Gökalp, An Evaluation of the Klimov-Williams Criterion, Combust. Flame 67 (1987), pp. 111–119.

[2] F. A. Williams, Criteria for existence of wrinkled laminar flame structure of turbulent premixed flames, Combust. Flame 26 (1976), pp. 269–270.

[3] R. Borghi, On the Structure and Morphology of Turbulent Premixed Flames, in C. Casci, C. Bruno (Eds.), Recent Advances in the Aerospace Science, Plenum Press, New York, 1985, pp. 117–138 ISBN: 978-1-4684-4298-4.

[4] N. Peters, Laminar flamelet concepts in turbulent combustion, Proc. Combust. Inst. 21 (1988), pp. 1231–1250.

[5] R. G. Abdel-Gayed, D. Bradley, F. K.-K. Lung, Combustion Regimes and the Straining of Turbulent Premixed Flames, Combust. Flame 76 (1989), pp. 213–218.

[6] T. Poinsot, D. Veynante, S. Candel, Quenching processes and premixed turbulent combustion diagrams, J. Fluid Mech. 228 (1991), pp. 561–606.

[7] N. Peters, The turbulent burning velocity for large-scale and small-scale turbulence, J. Fluid Mech. 384 (1999), pp. 107–132.

[8] K. N. C. Bray, Laminar Flamelets and the Bray, Moss, and Libby Model, in N. Swaminathan, K. N. C. Bray (Eds.), Turbulent Premixed Flames, Cambridge University Press, 2011, pp. 41–60, ISBN: 978-0-521-76961-7.

[9] Y. Minamoto, N. Swaminathan, R. S. Cant, T. Leung, Reaction Zones and Their Structure in MILD Combustion, Combust. Sci. Technol. 186 (2014) pp. 1075–1096.

[10] T. Plessing, N. Peters, J. G. Wünning, Laseroptical investigation of highly preheated combustion with strong exhaust gas recirculation, Proc. Combust. Inst. 27 (1998), pp. 3197–3204.

[11] K. H. H. Goh, P. Geipel, F. Hampp, R. P. Lindstedt, Regime transition from premixed to flameless oxidation in turbulent JP-10 flames, Proc. Combust. Inst. 34, (2013), pp. 3311–3318.

[12] K. H. H. Goh, P. Geipel, R. P. Lindstedt, Turbulent transport in premixed flames approaching extinction, Proc. Combust. Inst. 35 (2015), pp. 1469–1476.

[13] C. Duwig, B. Li, Z. S. Li, M. Aldén, High resolution imaging of flameless and distributed turbulent combustion, Combust. Flame 159 (2012), pp. 306–316.

[14] V. D. Milosavljevic, R. P. Lindstedt, M. D. Cornwell, E. J. Gutmark, E. M. Váos, Combustion Instabilities Near the Lean Extinction Limit, in G. Roy, K. H. Yu, J. H. Whitelaw, J. J. Witton (Eds.), Advances in Combustion and Noise Control, Cranfield University Press, 2006, pp. 149–165.

[15] B. Zhou, C. Brackmann, Z. Li, M. Aldén, X.-S. Bai, Simultaneous multi-species and temperature visualization of premixed flames in the distributed reaction zone regime, Proc. Combust. Inst. 35 (2015), pp. 1409–1416.

[16] B. Zhou, C. Brackmann, Q. Li, Z. Wang, P. Petersson, Z. Li, M. Aldén, X.-S. Bai, Distributed reactions in highly turbulent premixed methane/air flames. Part I. Flame structure characterization, Combust. Flame 162 (2015), pp. 2937–2953.

[17] B. Zhou, Q. Li, Y. He, P. Petersson, Z. Li, M. Aldén, X.-S. Bai, Visualization of multi-regime turbulent combustion in swirl-stabilized lean premixed flames, Combust. Flame 162 (2015), pp. 2954–2958.

[18] B. Zhou, C. Brackmann, Z. Wang, Z. Li, M. Richter, M. Aldén, X.-S. Bai, Thin reaction zone and distributed reaction zone regimes in turbulent premixed methane/air flames: Scalar distributions and correlations, Combust. Flame (2016), http://dx.doi.org/10.1016/j.combustflame.2016.06.016.

[19] A. W. Skiba, T. M. Wabel, C. D. Carter, S. D. Hammack, J. E. Temme, T. Lee, J. F. Driscoll, Reaction layer visualization: A comparison of two PLIF techniques and advantages of kHz-imaging, Proc. Comb. Inst. (2016), http://dx.doi.org/10.1016/j.proci.2016.07.033.

[20] T. M. Wabel, A. W. Skiba, J. F. Driscoll, Turbulent burning velocity measurements: Extended to extreme levels of turbulence, Proc. Comb. Inst. (2016), http://dx.doi.org/10.1016/j.proci.2016.08.013.

[21] T. M. Wabel, A. W. Skiba, J. E. Temme, J. F. Driscoll, Measurements to determine the regimes of premixed flames in extreme turbulence, Proc. Comb. Inst. (2016), http://dx.doi.org/10.1016/j.proci.2016.08.065.

[22] Y. Minamoto, T. D. Dunstan, N. Swaminathan, R. S. Cant, DNS of EGR-type turbulent flame in MILD condition, Proc. Combust. Inst. 34 (2013), pp. 3231–3238.

[23] Y. Minamoto, N. Swaminathan, Scalar gradient behaviour in MILD combustion, Combust. Flame 161 (2014), pp. 1063–1075.

[24] S. Lapointe, B. Savard, G. Blanquart, Differential diffusion effects, distributed burning, and local extinctions in high Karlovitz premixed flames, Comb. Flame 162 (2015), pp. 3341–3355.

[25] A. W. Skiba, T. M. Wabel, J. E. Temme, J. F. Driscoll, Experimental Assessment of Premixed Flames Subjected to Extreme Turbulence, AIAA 54 (2016) 1454.

[26] E. Mastorakos, A. M. K. P. Taylor, J. H. Whitelaw, Extinction of Turbulent Counterflow Flames with Reactants Diluted by Hot Products, Combust. Flame 102 (1995), pp. 101–114.

[27] K. H. H. Goh, Investigation of Conditional Statistics in Premixed Combustion and the Transition to Flameless Oxidation in Turbulent Opposed Jets, PhD thesis, Imperial College, Aug 2013, url: http://hdl.handle.net/10044/1/28073.

[28] B. Coriton, M. D. Smooke, A. Gomez, Effect of the composition of the hot product stream in the quasi-steady extinction of strained premixed flames, Combust. Flame 157 (2010), pp. 2155–2164.

[29] B. Coriton, J. H. Frank, A. Gomez, Effects of strain rate, turbulence, reactant stoichiometry and heat losses on the interaction of turbulent premixed flames with stoichiometric counterflowing combustion products, Combust. Flame 160 (2013), pp. 2442–2456.

[30] P. Geipel, K. H. H. Goh, R. P. Lindstedt, Fractal-Generated Turbulence in Opposed Jet Flows, Flow Turbul. Combust. 85 (2010), pp. 397–419.

[31] B. Böhm, O. Stein, A. Kempf, A. Dreizler, In-Nozzle Measurements of a Turbulent Opposed Jet using PIV, Flow Turbul. Combust. 85 (2010), pp. 73–93.

[32] D. Geyer, A. Kempf, A. Dreizler, J. Janicka, Turbulent opposed-jet flames: A critical benchmark experiment for combustion LES, Combust. Flame 143 (2005), pp. 524–548.

[33] K. H. H. Goh, P. Geipel, R. P. Lindstedt, Lean premixed opposed jet flames in fractal grid generated multiscale turbulence, Combust. Flame 161 (2014), pp. 2419–2434.

[34] K. H. H. Goh, P. Geipel, F. Hampp, R. P. Lindstedt, Flames in fractal grid generated turbulence, Fluid Dyn. Res. 45, (2013), 061403.

[35] D. Hurst, J. C. Vassilicos, Scalings and decay of fractal-generated turbulence, Phys. Fluids 19 (2007), 035103.

[36] R. E. Seoud, J. C. Vassilicos, Dissipation and decay of fractal-generated turbulence, Phys. Fluids 19 (2007), 105108.

[37] P. Allison, Y. Chen, J. F. Driscoll, Investigation of Dimethyl Ether Combustion Instabilities in a Partially-Premixed Gas Turbine Model Combustor Using High-Speed Laser Diagnostics, AIAA 52 (2014), DOI: 10.2514/6.2014-0660.

[38] C. Arcoumanis, C. Bae, R. Crookes, E. Kinoshita, The potential of di-methyl ether (DME) as an alternative fuel for compression-ignition engines: A review, Fuel 87 (2008), pp. 1014–1030.

[39] Y. L. Wang, A. T. Holley, C. Ji, F. N. Egolfopoulos, T. T. Tsotsis, H. J. Curran, Propagation and extinction of premixed dimethyl-ether/air flames, Proc. Combust. Inst. 32 (2009), pp. 1035–1042.

[40] S. L. Fischer, F. L. Dryer, H. J. Curran, The reaction kinetics of dimethyl ether. I: High-temperature pyrolysis and oxidation in flow reactors, Int. J. Chem. Kinet. 32 (2000), pp. 713–740.

[41] F. Fuest, R. S. Barlow, J. Y. Chen, A. Dreizler, Raman/Rayleigh scattering and CO-LIF measurements in laminar and turbulent jet flames of dimethyl ether, Combust. Flame 159 (2012), pp. 2533–2562.

[42] F. Fuest, G. Magnotti, R. S. Barlow, J. A. Sutton, Scalar structure of turbulent partially-premixed dimethyl ether/air jet flames, Proc. Combust. Inst. 35 (2015), pp. 1235–1242.

[43] K. N. Gabet, H. Shen, R. A. Patton, F. Fuest, J. A. Sutton, A comparison of turbulent dimethyl ether and methane non-premixed flame structure, Proc. Combust. Inst. 34 (2013), pp. 1447–1454.

[44] F. Hampp, R. P. Lindstedt, Strain distribution on material surfaces during combustion regime transitions, Proc. Combust. Inst. (2016), http://dx.doi.org/10.1016/j.proci.2016.07.018.

[45] D. B. Spalding, Multi-fluid models of turbulent combustion, Proc. Seventh Biennial Conf. on Comp. Techn. Applications (CTAC 95), World Scientific Publishing Co Ltd, (1996) pp. 59–81.

[46] F. Hampp, R. P. Lindstedt, Fractal Grid Generated Turbulence - A Bridge to Practical Combustion Applications, in Y. Sakai and C. Vassilicos (eds.) Fractal Flow Design: How to Design Bespoke Turbulence and why, Springer-Verlag, CISM Int. Mech. Sci. 568, 2016, DOI:10.1007/978-3-319-33310-6 3.

[47] G. Coppola, A. Gomez, Experimental investigation on a turbulence generation system with high-blockage plates, Exp. Therm. Fluid Sci. 33 (2009), pp. 1037–1048.

[48] F. Hampp, Quantification of Combustion Regime Transitions, PhD thesis, Imperial College, May 2016, url: http://hdl.handle.net/10044/1/32582.

[49] J. Kerl, T. Sponfeldner, F. Beyrau, An external Raman laser for combustion diagnostics, Combust. Flame 158 (2011), pp. 1905–1907.

[50] P. Černý, H. Jelinková, P. G. Zverev, T. T. Basiev, Solid state lasers with Raman frequency conversion, Prog. Quant. Electron. 28 (2004), pp. 113–143.

[51] M. Raffel, C. E. Willert, S. Wereley, J. Kompenhans, Particle Image Velocimetry, Springer Verlag, Berlin, 2007, ISBN: 978-3-642-43166-1.

[52] D. Han, M. G. Mungal, Simultaneous measurements of velocity and CH distributions. Part 1: Jet flames in co-flow, Combust. Flame 132 (2003), pp. 565–590.

[53] A. Melling, Tracer particles and seeding for particle image velocimetry, Meas. Sci. Technol. 8 (1997), pp. 1406–1416.

[54] K. P. Angele, B. Muhammad-Klingmann, A simple model for the effect of peak-locking on the accuracy of boundary layer turbulence statistics in digital PIV, Exp. Fluids 38 (2005), pp. 341–347.

[55] LaVision, FlowMaster Product Manual for Davis 8.3, LaVision GmbH, Göttingen, Germany, 9^{th} August (2016), Item-Number: 1105011–4.

[56] B. Wieneke, K. Pfeiffer, Adaptive PIV with variable interrogation window size and shape, 15^{th} Int. Symp. Appl. Laser Tech. Fluid Mech. (2010), url: http://ltces.dem.ist.utl.pt/LXLASER/lxlaser2010/upload/1845_qkuqls_1.12.3.Full_1845.pdf.

[57] B. Wieneke, Private communication on adaptive PIV calculations, 31 March 2017.

[58] R. J. Adrian, Dynamic ranges of velocity and spatial resolution of particle image velocimetry, Meas. Sci. Technol. 8 (1997), pp. 1393–1398.

[59] F. Scarano, Development and Assessment of Non-Isotropic Spatial Resolution PIV, in M. Stanislas, J. Westerweel, J. Kompenhans (eds.) Particle Image Velocimetry: Recent Improvements, Springer Verlag, Proc. EUROPIV 2^{nd} Workshop, Zaragoza, Spain (2003), DOI 10.1007/978-3-642-18795-7.

[60] M. Raffel, J. Kompenhans, Error analysis for PIV recording utilizing image shifting. 7^{th} Int. Symp. Appl. Laser Tech. Fluid Mech., Lisbon, Portugal, July (1994).

[61] A. Gomez, D. E. Rosner, Thermophoretic Effects on Particles in Counterflow Laminar Diffusion Flames, Combust. Sci. Technol. 89 (1993), pp. 335–362.

[62] A. Stella, G. Guj, J. Kompenhans, M. Raffel, H. Richard, Application of particle image velocimetry to combusting flows: design considerations and uncertainty assessment, Exp. Fluids 30 (2001), pp. 167–180.

[63] B. Wieneke, Generic a-posteriori uncertainty quantification for PIV vector fields by correlation statistics, 17^{th} Int. Symp. Appl. Laser Tech. Fluid Mech., Lisbon, Portugal, 07-10 July (2014).

[64] J. Westerweel, F. Scarano, Universal outlier detection for PIV data, Exp Fluids 39 (2005) pp. 1096–1100.

[65] A. Haar, Zur Theorie der orthogonalen Funktionensysteme, Math. Ann. 69 (1910), pp. 331–371.

[66] S.-W. Park, Detailed Chemical Kinetic Model for Oxygenated Fuels, PhD thesis, Imperial College, March 2012, url: http://hdl.handle.net/10044/1/9599.

[67] H. J. Curran, W. J. Pitz, C. K. Westbrook, P. Dagaut, J. C. Boettner, M. Cathonnet, A Wide Range Modeling Study of Dimethyl Ether Oxidation, Int. J. Chem. Kinet. 30 (1998), pp. 229–241.

[68] M. P. Burke, M. Chaos, Y. Ju, F. L. Dryer, S. J. Klippenstein, Comprehensive H_2/O_2 kinetic model for high-pressure combustion, Int. J. Chem. Kinet., 44 (2012), pp. 444–474.

[69] X. Qin, Y. Ju, Measurements of burning velocities of dimethyl ether and air premixed flames at elevated pressures, Proc. Combust. Inst. 30 (2005), pp. 233–240.

[70] J. de Vries, W. B. Lowry, Z. Serinyel, H. J. Curran, E. L. Petersen, Laminar flame speed measurements of dimethyl ether in air at pressures up to 10 atm, Fuel, 90 (2011), pp. 331–338.

[71] T. A. Cool, J. Wang, N. Hansen, P. R. Westmoreland, F. L. Dryer, Z. Zhao, A. Kazakov, T. Kasper, K. Kohse-Höinghaus, Photoionization mass spectrometry and modeling studies of the chemistry of fuel-rich dimethyl ether flames, Proc. Combust. Inst. 31 (2007), pp. 285–293.

[72] J. Wang, M. Chaos, B. Yang, T. A. Cool, F. L. Dryer, T. Kasper, N. Hansen, P. Oßwald, K. Kohse-Höinghaus, P. R. Westmoreland, Composition of reaction intermediates for stoichiometric and fuel-rich dimethyl ether flames: flame-sampling mass spectrometry and modeling studies, Phys. Chem. Chem. Phys. 11 (2009), pp. 1328–1339.

[73] R. D. Cook, D. F. Davidson, R. K. Hanson, Shock tube measurements of ignition delay times and OH time-histories in dimethyl ether oxidation, Proc. Combust. Inst. 32 (2009), pp. 189–196.

[74] C. Tang, L. Wei, J. Zhang, X. Man, Z. Huang, Shock Tube Measurements and Kinetic Investigation on the Ignition Delay Times of Methane/Dimethyl Ether Mixtures, Energy Fuels 26 (2012), pp. 6720–6728.

[75] L. Pan, E. Hu, J. Zhang, Z. Zhang, Z. Huang, Experimental and kinetic study on ignition delay times of DME/H_2/O_2/Ar mixtures, Combust. Flame 161 (2014), pp. 735–747.

[76] W. P. Jones, R. P. Lindstedt, The Calculation of the Structure of Laminar Counterflow Diffusion Flames Using a Global Reaction Mechanism, Combust. Sci. Techn. 61 (1988), pp. 31–49.

[77] N. Peters, Kinetic foundation of thermal flame theory, in W. A. Sirignano, A. G. Merzhanov, L. de Luca (Eds.), Advances in Combustion Science: In Honor of Y. B. Zel'dovich, Prog. Astronautics and Aeronautics 173 (1997) pp. 73–91.

[78] Z. S. Li, B. Li, Z. W. Sun, X. S. Bai, M. Aldén, Turbulence and combustion interaction: High resolution local flame front structure visualization using simultaneous single-shot PLIF imaging of CH, OH, and CH_2O in a piloted premixed jet flame, Combust. Flame 157 (2010) pp. 1087–1096.

[79] F. Dinkelacker, A. Soika, D. Most, D. Hofmann, A. Leipertz, W. Polifke, K. Döbbeling, Structure of locally quenched highly turbulent lean premixed flames, Proc. Combust. Inst. 27 (1998) pp. 857–865.

[80] F. T. C. Yuen, Ö. L. Gülder, Premixed turbulent flame front structure investigation by Rayleigh scattering in the thin reaction zone regime, Proc. Combust. Inst. 32 (2009) pp. 1747–1754.

[81] J. F. Driscoll, Turbulent premixed combustion: Flamelet structure and its effect on turbulent burning velocities, Prog. Energy Combust. Sci. 34 (2008) pp. 91–134.

[82] M. J. Dunn, A. R. Masri, R. W. Bilger, R. S. Barlow, G.-H. Wang, The compositional structure of highly turbulent piloted premixed flames issuing into a hot coflow, Proc. Combust. Inst. 32 (2009) pp. 1779–1786.

[83] J. Savre, H. Carlsson, X. S. Bai, Tubulent Methane/Air Premixed Flame Structure at High Karlovitz Numbers, Flow Turbul. Combust. 90 (2013) pp. 325–341.

[84] B. Böhm, C. Heeger, I. Boxx, W. Meier, A. Dreizler, Time-resolved conditional flow field statistics in extinguishing turbulent opposed jet flames using simultaneous highspeed PIV/OH-PLIF, Proc. Combust. Inst. 32 (2009), pp. 1647–1654.

[85] I. G. Shepherd, R. K. Cheng, P. J. Goix, The spatial scalar structure of premixed turbulent stagnation point flames, Proc. Combust. Inst. 23 (1991), pp. 781–787.

[86] A. M. Steinberg, J. F. Driscoll, S. L. Ceccio, Measurements of turbulent premixed flame dynamics using cinema stereoscopic PIV, Exp. Fluids 44 (2008), pp. 985–999.

[87] R. C. Gonzalez, R. E. Woods, S. L. Eddins, Digital Image Processing Using MATLAB, New Jersey, Pearson Prentice Hall, 2004.

[88] B. Fond, C. Abram, F. Beyrau, On the characterisation of tracer particles for thermographic particle image velocimetry, Appl. Phys. B 118 (2015), pp. 393–399.

[89] W. Thielicke, E. J. Stamhuis, PIVlab – Towards User-friendly, Affordable and Accurate Digital Particle Image Velocimetry in MATLAB, J. Open Res. Soft. 2 (2014), doi:http://dx.doi.org/10.5334/jors.bl.

[90] F. J. Weinberg, The Shadowgraph of a Flat Flame, Proc. R. Soc. Lond. A 235 (1956), pp. 510–517.

[91] J. M. Seitzman, R. K. Hanson, Comparison of Excitation Techniques for Quantitative Fluorescence Imaging of Reacting Flows, AIAA 31 (1993), pp. 513–519.

[92] B. E. Battles, R. K. Hanson, Laser-induced fluorescence measurements of NO and OH mole fraction in fuel-lean, high-pressure (1–10 atm) methane flames: Fluorescence modeling and experimental validation, J. Quant. Spectrosc. Radiat. Transfer 54 (1995), pp. 521–537.

[93] J. Luque, D. R. Crosley, LIFBASE Spectroscopy Tool, 2015.

[94] N. L. Garland, D. R. Crosley, On the collisional quenching of electronically excited OH, NH and CH in flames, Proc. Combust. Inst. 21 (1988), pp. 1693–1702.

[95] G. P. Smith, D. R. Crosley, Quenching of OH ($A^2\Sigma^+$, v' = 0) by H_2, N_2O, and hydrocarbons at elevated temperatures, J. Chem. Phys. 85 (1986), pp. 3896–3901.

[96] Armed Forces Supply Support Center, Photographic Lenses, Washington 25 D.C., Tech. Rep. MIL-STD-150A, (1963).

[97] K. A. Buch, W. J. A. Dahm, Experimental study of the fine-scale structure of conserved scalar mixing in turbulent shear flows. Part 2. Sc = 1, J. Fluid Mech. 364 (1998) pp. 1–29.

[98] G. K. Batchelor, Small-scale variation of convected quantities like temperature in turbulent fluid Part 1. General discussion and the case of small conductivity, J. Fluid Mech. 5 (1959) pp. 113–133.

[99] I. G. Shepherd, J. B. Moss, K. N. C. Bray, Turbulent transport in a confined premixed flame, Proc. Combust. Inst. 19 (1982) pp. 423–431.

[100] P. Petersson, J. Olofsson, C. Brackman, H. Seyfried, J. Zetterberg, M. Richter, M. Aldén, M. A. Linne, R. K. Cheng, A. Nauert, D. Geyer, A. Dreizler, Simultaneous PIV/OH-PLIF, Rayleigh thermometry/OH-PLIF and stereo PIV measurements in a low-swirl flame, Appl. Optics 46 (2007) pp. 3928–3936.

[101] B. Böhm, D. Geyer, A. Dreizler, K. K. Venkatesan, N. M. Laurendeau, M. W. Renfro, Simultaneous PIV/PTV/OH PLIF imaging: Conditional flow field statistics in partially premixed turbulent opposed jet flames, Proc. Combust. Inst. 31 (2007) pp. 709–717.

[102] W. K. George, H. J. Hussein, Locally axisymmetric turbulence, J. Fluid Mech. 233 (1991), pp. 1–23.

[103] L. W. Kostiuk, K. N. C. Bray, T. C. Chew, Premixed Turbulent Combustion In Counterflowing Streams, Combust. Sci. Technol. 64 (1989) pp. 233–241.

[104] C. J. Lawn, R. W. Schefer, Scaling of premixed turbulent flames in the corrugated regime, Combust. Flame 146 (2006) pp. 180–199.